



**University of
Nottingham**
UK | CHINA | MALAYSIA

INVESTIGATING THE STRUCTURE-FUNCTION RELATIONSHIP OF THE HUMAN BRAIN USING HIGH-RESOLUTION CONNECTOMES

7,917 words

By Reece Hill

Computational Neuroscience, Cognition and A.I. (Masters of Science).

School of Psychology, University of Nottingham, UK.

2021-22

ABSTRACT

Background

Connectomes effect brain function and map how neurones are wired together. High-resolution connectomes ($>50,000$ nodes) have recently been shown to be reliably and reproducibly reconstructed from magnetic resonance images (MRI). Further brain properties are revealed in this way, especially intra-areal. Work is required to understand how brain function is related to the connectome, and no previous studies have investigated this at high resolution.

Purpose

To evaluate the structure-function relationship of the brain. Specifically left and right precentral gyri, sites of the motor homunculus. Two cortical maps are considered: one of function, from functional MRI (fMRI); and the structural connectome's. This study's primary purpose is to compare these maps, or put otherwise, the similarity of brain function to the circuitry that underpins it.

Methods

MRI data of healthy adults ($n=12$) were collected from the Individual Brain Charting dataset. The brain's surface was parcellated into $>50,000$ nodes, and deterministic fibre-tracking methods were applied to diffusion-MRI. These tracts produced a binary connectivity matrix, and its modularity was determined by Louvain community-detection algorithm. fMRIs of five motor tasks are compared to this: hand and foot (left/right) and tongue movements. How well the two mappings overlay was measured.

Results

Inter-individual and inter-task variation was observed. Without distinction of task or participant, but comparing only best-aligning module combinations for each case, structural module coverage by fMRI was moderate-poor (mean=40.87%; SD=17.68%).

Conclusion

Structural connectomes impose some constraint on brain function topology. There is an exceptional need for further refinement of methodology and improved literature base.

Word count: 249

LIST OF CONTENTS

1	Introduction	8
2	An introduction to connectomics.....	9
2.1	From inception to current use	9
2.2	Methods of connectome reconstruction	12
2.2.1	Invasive: sTEM and sSEM.....	13
2.2.2	Non-invasive: neuroimaging	14
2.3	The connectome as a network: nodes, edges, hubs, and modules	16
3	Methodology.....	18
3.1	Data acquisition.....	18
3.1.1	Functional task MRI (task-fMRI).....	19
3.2	Data processing	20
3.2.1	Finding and defining structural modules.....	21
3.2.2	Finding and defining functional modules.....	25
4	Results	32
4.1	Larger functional modules arise from more structural modules	32
4.2	Strength of alignment of functional modules to structural modules is weak-moderate and dependent on motor-task	34
4.3	Coverage of structural modules by functional modules shows little inter-individual variation	36
5	Discussion.....	36
5.1	Statistical limitations.....	37
5.2	Limitations of reconstruction using DTI.....	37
5.3	Limitations of reconstruction using fMRI	38
6	Conclusion	39
7	Appendix A.....	47
7.1	Search queries for literature reviews.....	47
7.1.1	Nanoconnectomes	47
7.1.2	Connectomes	47
8	Appendix B.....	48

8.1	Participant information	48
9	Appendix C	49
9.1	MRI scanning protocols	49
9.1.1	High-resolution diffusion data.....	49
9.1.2	High-resolution T1 data.....	49
9.1.3	T2 SPC data.....	50
9.1.4	fMRI data for all motor tasks	50
10	Appendix D	51
10.1	Connectivity matrices	51
11	Appendix E	53
11.1	Structural and functional modules per participant	53
12	Appendix F	65
12.1	Distribution of quantity of all functional and structural modules	65
12.2	Normalised coverage of <i>fy</i> over <i>sx</i> per subject by condition.....	66
13	Acknowledgements.....	67

LIST OF FIGURES

Figure 1: The motor homunculus.....	8
Figure 2: Scaling connectomics reconstruction from a Worm to a Mouse.....	10
Figure 3: Parcellations protocols of the brain.....	11
Figure 4: The ten spatial scales of connectomic investigations.....	12
Figure 5: Transmission electron microscopy (TEM) and scanning electron microscopy (SEM).....	13
Figure 6: A tractography-generated, structural, human connectome.....	15
Figure 7: Basic network attributes.....	16
Figure 8: Examples of random, small-world and lattice network topology.....	17
Figure 9: Schematic of fMRI block-design experiment.....	19
Figure 10: Images shown to participants to instruct desired bodily “tapping” movements.....	20
Figure 11: Methodology summary.....	20
Figure 12: High-resolution global connectivity matrix.....	22
Figure 13: Reordered local connectivity matrix of left precentral gyrus.....	24
Figure 14: Structural modules of precentral gyri.....	25
Figure 15: The contrast used in SPM12 for the “left hand” motor task.....	27
Figure 16: The output from SPM’s GLM.....	28
Figure 17: The effect of volume size on vol2surf.....	28
Figure 18: Histogram showing the mean distances of modules’ voxels from their nearest cortical surface node for all participants.....	29
Figure 19: Functional modules of a single participant’s precentral gyri.....	29
Figure 20: A schematic of a portion of the precentral gyrus surface.....	30
Figure 21: Distribution of number of structural modules per $f *$ by motor task.....	32
Figure 22: Boxplot showing surface area size in squared millimetres of $(sx \cap fy)$, fy and sx , respectively, for all motor tasks.....	33
Figure 23: Boxplots showing the normalised, weighted mean of all optimal functional module’s ($f *$) coverage, i , of their underlying structural modules (sx).....	34
Figure 24: Boxplots for each participant, showing the distribution of their functional modules’ (f_y) overlap with underlying structural modules (i).....	36

LIST OF TABLES

Table 1: Results of one-sample t-test ($\alpha=0.05$), comparing present i against published correlation score of 0.416.....	34
Table 2: Results of one-sample t-test ($\alpha=0.05$), comparing i of the tongue against published correlation score of 0.43.....	35
Table 3: Participant demographics.....	48

LIST OF ABBREVIATIONS

<u>Abbreviation</u>	<u>Description</u>
AC	Anterior commissure. An anatomical landmark of the human brain. A white matter tract that connects the two temporal lobes across the midline.
ATUM	Automated tape-collecting ultramicrotome. A method of preparing and storing thinly sliced microscope slides.
DSI (Studio)	A software package that maps brain connections (tractography).
DTI	Diffusion tensor imaging/images. A subtype of diffusion-weighted images,
DWI	Diffusion weighted imaging/images. A type of magnetic resonance imaging.
EEG	Electroencephalogram. A recording of electrical brain activity using probes placed on the scalp.
FWE	Family-wise error. A method of correcting fMRI results by performing statistics at a cluster-level, rather than voxel.
GLM	General Linear Model.
HCP	Human Connectome Project.
IBC	Individual Brain Charting.
IQ	Intelligence Quotient.
MATLAB	A programming platform.
MEG	Magnetoencephalography. A recording of changes in the brain's magnetic field.
MNI	Montreal Neurological Institute space. A standardised space made of usually 152 subject data.
MRI	Magnetic resonance images/images.
SD	Standard deviation.
SEM	Scanning electron microscopy/microscope.
SPM	Statistical Parametric Mapping. Software package written in MATLAB.
T1	MRI scanning sequence to acquire anatomical data.
T2	MRI scanning sequence to acquire anatomical data.
TB	Terabyte. A unit of digital storage space.
TEM	Transmission electron microscopy/microscope.

1 INTRODUCTION

The *connectome* is an umbrella term describing inter- and intra-areal brain connectivity. Conceptually, it is like the electrician's circuit diagram, except the human connectome exhibits plasticity and is unique to the individual. This dissertation takes magnetic resonance images (MRIs) and diffusion-weighted MRIs (dwMRIs) of 12 human participants and reconstructs their structural connectomes. If we know how the brain is wired, one would assume that we can extrapolate activity; two brain areas can only co-activate if they are directly, or indirectly, connected. Some papers have indicated that coarse intra-areal connectomes and functional networks are only moderately correlated ($r=0.416$, $p=0$) (Cocchi et al., 2014; Gu et al., 2021). Sarwar et al., however, used a feed-forward neural network to predict brain function from structure. Their relative success (individual: $r=0.55\pm0.1$; cohort averaged: $r=0.9\pm0.1$) reveals that the two may be coupled tighter than once thought (2021). So, we ask to what degree does the structural connectome constrain function?

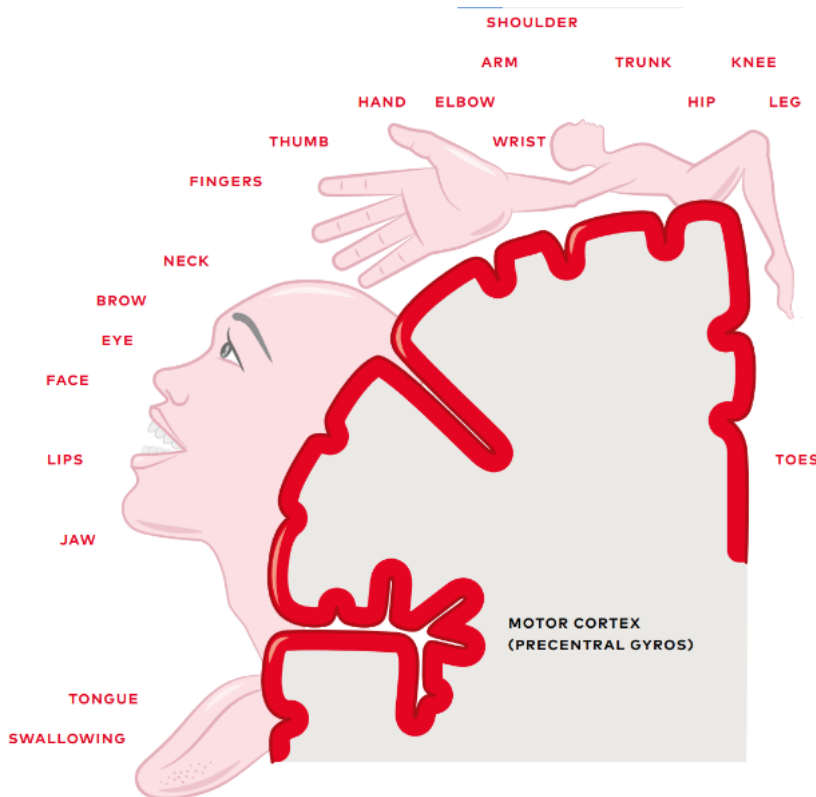


Figure 1: The motor homunculus, situated in the precentral gyrus of the right and left hemisphere (only right is shown). Adapted from (Nicholas, 2019).

To test this, we turn to the motor homunculus (Figure 1). This map of *functional topography* outlines the cortical neurones responsible for the movement of body parts. By using functional MRIs (fMRIs) that indirectly measure brain activity, one reveals pieces of an individual's functional map. More specifically,

for each of our 12 participants we yield brain areas of activity in response to five motor tasks: hand movement (left and right), foot movement (left and right), and tongue movement. We compare these to the individuals' structural connectomes. Does it follow that the functional area assigned to hand movement, for example, shows consistent overlap with a particular portion of the brain's wiring?

We extend upon the work of Taylor et al. to answer this question (2017). They found that cortical areas, including the precentral gyrus (the site of the motor homunculus), can be divided into clusters of densely connected neurones, or *modules*. We investigate these spatially localised sites, analogous to sub-portions of a circuit diagram, to see if they correlate to areas of the motor homunculus. For this endeavour, we use bespoke code and processing pipelines to bring together high-resolution structural connectomes and fMRI data. To the best of our knowledge, this is the first study to inspect intra-areal connectivity in this way.

2 AN INTRODUCTION TO CONNECTOMICS

2.1 FROM INCEPTION TO CURRENT USE

Although the term connectome was first coined in 2005 (Sporns et al.), the study of anatomical circuitry is not new. Nicolas Steensen, a scientist famous for discovering that the heart was made solely of muscle (Clarke, 1965), was also a keen neuroanatomist. In his 1665 lecture, "The Anatomy of the Brain", he proposed that studies investigating neurological disease had to break free from paradigms of animal spirits, and move towards more complex models (Parent, 2013). In particular, he expressed need for the study of white matter fibres, proclaiming "anatomy first, then physiology" (Steensen & Andrault, 2009). Ahead of his time, Steensen was calling for the study of connectomes, or *connectomics*.

More than 200 years later and with the advent of staining techniques able to demarcate neurones, Maynert put this into action in 1886. He documented the origin and destination of gross cortical fibres in the human brain. He proposed that the fibres connecting areas together, "association systems", were fundamental in the pathophysiology of mental illness (Maynert, 2018). His work aligned with the inquiry set before him by Steensen, although Maynert went further to imply psychiatric disease could be rooted in dysfunctional connectivity between brain areas. In fact, sole inspection of these inter-areal projections is akin to the subdivision of the connectome recently nicknamed the *projectome* (Kasthuri & Lichtman, 2007). A novel idea, though the greatest turning point in the field was yet to occur.

The true birth of connectomics is more recent (Abbott et al., 2020). Researchers used serial transmission electron microscopy (sTEM) to reconstruct the entire central nervous system of the nematode worm, *Caenorhabditis elegans* (White et al., 1986). They took serial, transverse sections, each ~50nm thick, and painstakingly traced the branches of every neurone. This was the first work of its type, commendable because it was done mostly by hand. Without today's computer or image processing algorithms, the

scientists produced a 340-page publication on the structure and organisation of the *C. elegans*' nervous system. It explored how this could affect "The Mind of a Worm", the authors' principle focus (White et al., 1986). This work has since inspired an era of connectomics with computer scientists, neuroscientists, and physicists, amongst many others, working together.

Improved technological power and processing standards have enabled researchers to automate their efforts. Now, organisms with larger and more complex nervous systems are the focus. In only a decade we have progressed from mapping specific circuits and regions of interests, such as the medulla of the *Drosophila melanogaster* fruit fly (Takemura et al., 2013), and the mouse retina (Helmstaedter et al., 2013), to the beginnings of whole-brain mapping (Abbott et al., 2020; Scheffer et al., 2020; Zheng et al., 2018).

It follows that connectomics may also be applied to human brains. This is an enormous undertaking with its own challenges and technological limitations. Fruit flies make an enticing choice for researchers as their brain consists of only 200,000 neurones (Nitta & Sugie, 2022; Zheng et al., 2018). Handling the billions of neurones of the adult human brain, however, is computationally expensive. Completing the task in one researcher's lifetime is also practically impossible if using present day methods (Kleinfeld et al., 2011).

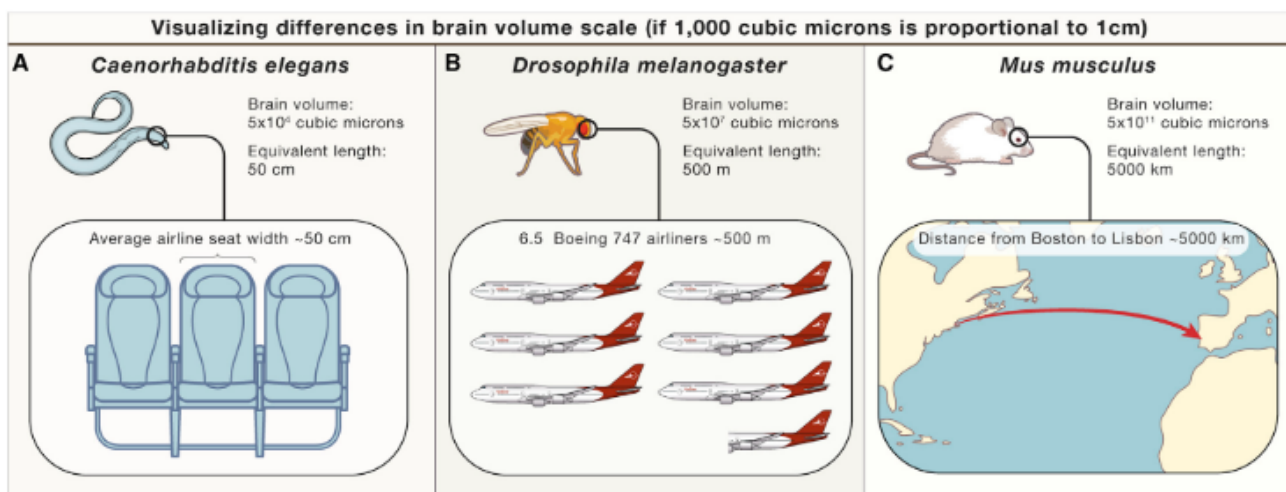


Figure 2: Scaling connectomics reconstruction from a Worm to a Mouse: A 10-million-fold increase in brain volume. Each 1,000 cubic microns of brain volume is schematically represented by a 1cm linear distance. Reproduced from (Abbott et al., 2020).

How much progress has been made? Around a decade ago, the mouse connectome was 10% complete (Mikula et al., 2012), and a call was made to expedite progress by improving collaboration amongst researchers (Bohland et al., 2009). Just last year, a seminal paper published 12.5% of the fruit fly's connectome, equating to ~25,000 neurones of its entire brain, and included some 20 million chemical synapses (Scheffer & Meinertzhagen, 2021). Understandably, the connectome in humans is similarly incomplete. Larger brain volumes equate to larger connectomes (Figure 2) and, as a result, often lack topological resolution. For these, parcellation-based representations are the current standard (Van Essen

& Ugurbil, 2012). Put simply, neurones are grouped together into *parcels* and these, fewer in number, are used in further computations and mathematics. This is termed a *parcellated connectome* (see: Methods of connectome reconstruction) (Van Essen, Ugurbil, et al., 2012).

The scientific community continues to discuss the optimal parcellation protocol, although two main schools of thought exist: parcels should share common cellular architecture, topography, and/or function; or, parcellation protocols ought to divide the brain into areas roughly equal in size (e.g., Figure 3). Whilst the former approach appears the most rigorous, how to divide the human cortex into areas remains debatable (Van Essen & Ugurbil, 2012). One study used a population average of 52 cortical areas for a sub portion of one hemisphere, and from this extrapolated 300-400 parcels per whole brain (Van Essen, Glasser, et al., 2012).

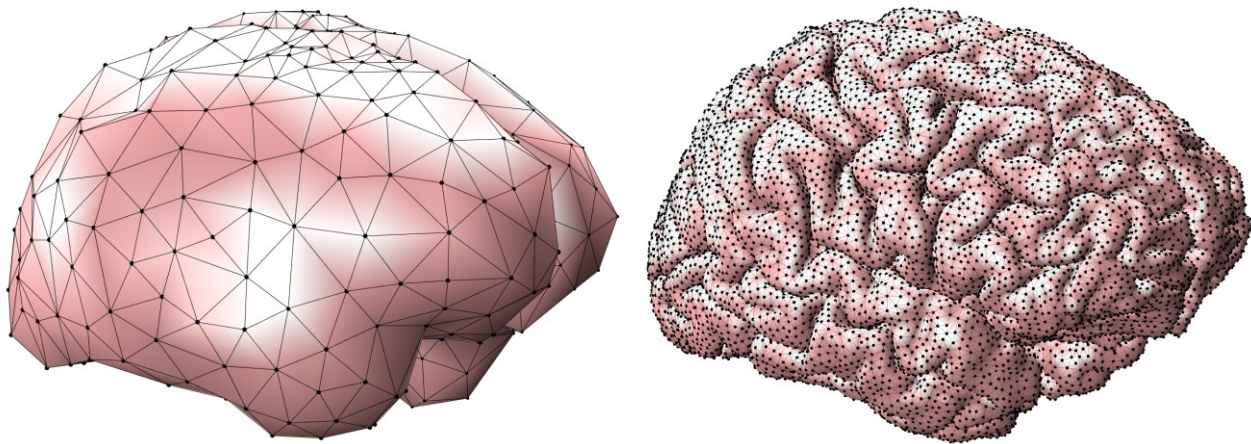


Figure 3: Left – parcellation of the human brain into 1,000 nodes, the usual representation found in literature. Right – parcellation of the brain into 50,000 nodes, a high-resolution approach presented in this paper. Both – triangles represent parcels, black dots are nodes, and the lines connecting them are edges.

Even still, most human connectomic studies opt for coarser parcellations where each parcel's size is normalised. The $2,400\text{cm}^2$ surface area of the entire cerebral cortex is commonly divided into a mere 100 parcels, although sometimes 1,000 (Figure 3, left). This method allows some investigation into connectivity. Mostly that between brain regions and global properties of the network. However, the granularity afforded by this method is insufficient to explore finer details. It is impossible, for example, to examine a single brain area and the connections within (i.e., intra-areal connectivity), as are studied here.

The preference for low-resolution was originally motivated by limitations in processing power; then, perpetuated by the lack of evidence for the reproducibility of finer parcellations (Taylor et al., 2017). 2014 evidence has since shown excellent inter-scan agreement of ten scans that were reconstructed into high-resolution parcellated connectomes of 58,880 parcels (Besson et al., 2014). This motivates our use of structural connectomes with $>50,000$ parcels, and we remind the reader that the best descriptions of brain circuitry arise from connectomes that are as finely parcellated as possible (Van Essen & Ugurbil, 2012).

2.2 METHODS OF CONNECTOME RECONSTRUCTION

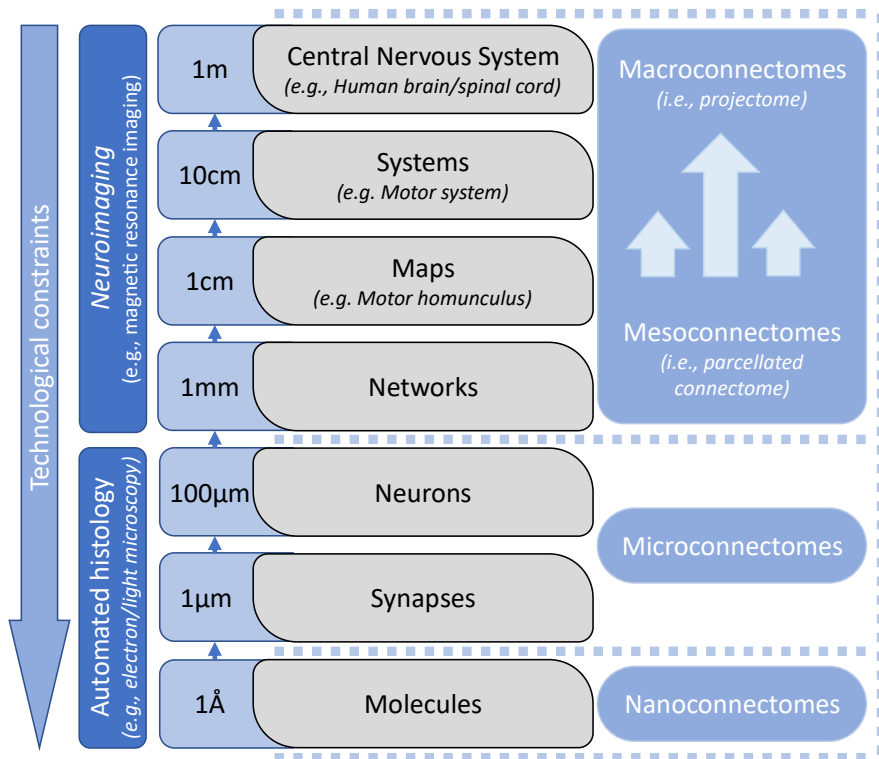


Figure 4: The ten spatial scales of connectomic investigations proposed by Churchland and Sejnowski (1988). Schematic has been adapted to include relevant methodology and examples for each scale, and alignment with nano-, micro-, meso- and macroconnectome terminology. Arrows between macro- and mesoconnectomes imply a gradient exists between the two terms.

It is impossible to capture the entire connectome at once because different spatial scales offer different properties, and no single data acquisition tool works at all resolutions. Connectomes exist across ten spatial scales (Figure 4). We introduce four sub-divisions of the connectome used in the literature that align with these scales: nano-, micro-, meso-, and macro-connectomes (Fornito et al., 2019). In this section, we further explore the complexity of measuring the connectome. This is in aid of placing our use of neuroimaging in context.

The *C. elegans* remains the only connectome that is complete at the microscopic scale of single neurons and synapses. Even smaller still is that of the nanoconnectome, where scientists use reconstructions at a near-molecular resolution. They investigate the constituents of neurones and their extracellular spaces. Principles of biochemistry (e.g., neuronal calcium influx) and stochastic events dominate at this level. Sejnowski recently applied nanoconnectomics to study the precision of synaptic plasticity within the human hippocampus. This preliminary study suggests that long-term memory formation relies upon effective synaptic processes that take place at a nanoscopic scale (Sejnowski, 2016). Other research into nanoscale connectomes is up and coming, though the field is relatively understudied compared to coarser scales (see Appendix A).

Returning to the mesoscale, there is the aforementioned parcellated connectome, which is where our study lies. However, the difference between meso- and macro-scale is not distinct, as represented in Figure 4 and identified by Sporns (2016). In fact, some authors identify parcellated connectomes as macroscale (de Reus & van den Heuvel, 2013). Anyhow, the two terms sit on opposing ends of a gradient in spatial resolution, with the projectome on the side of least resolution (macroscopy) and the parcellated connectome closer to mesoscopy, depending on parcellation protocol parameters (Sporns et al., 2005).

Also shown in Figure 4 is the issue of technological constraints. Studies of large connectomes (i.e., humans) are often forced to use higher levels of abstraction. The aim is to minimise the amount of data to be handled. Avoiding the storage and processing of the 10^{11} neurones of the human brain is an absolute requirement imposed by present day computing (Sporns et al., 2005). For reference, Ohno et al. report that for microscopic reconstruction (see: Figure 5, right), the *C. elegans*' connectome could generate data 3.1-25 terabytes (TB) in size, depending on desired resolution. For the mouse brain, this is upwards of 210,000TB (2015). We can already anticipate that the human brain would generate too much data if recorded at the microscopic level. Instead, researchers resort to higher orders of spatial scale. By using fMRI in a mouse study, researchers could expect to handle a very manageable 30 megabytes, approximately. Hence, we introduce neuroimaging as a perfect candidate for human connectomes.

2.2.1 Invasive: sTEM and sSEM

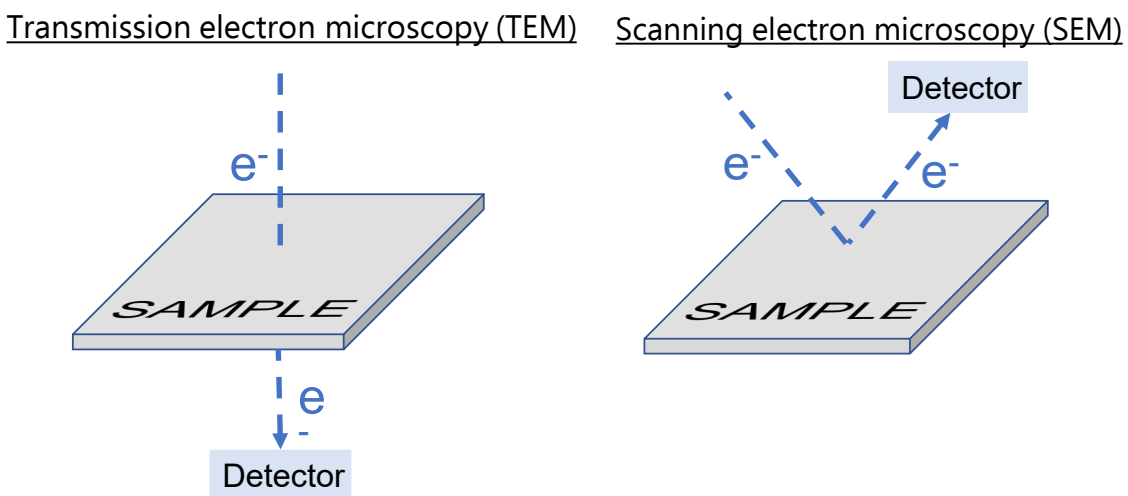


Figure 5: Left - transmission electron microscopy (TEM) works by detecting the electrons (e^-) that pass through the sample. Right – scanning electron microscopy (SEM) detects the electrons (e^-) that reflect from the sample's surface structures. When applied sequentially to slices of a volume, they become serial TEM (sTEM) and serial SEM (sSEM).

Ohno et al. go further to enforce that researchers must opt for different approaches to efficiently record connectomes of larger species (2015). Whilst the sTEM used to obtain the *C. elegans* connectome was a success and is a common technique, it is labour-intensive and prone to human error (Harris et al., 2006). It is inappropriate for human studies even if computers were to process the vast amounts of data. Its

resolution is insufficient for larger volumes of tissue, limited by the need for ultrathin specimens, cell stains, and manual cutting (Ohno et al., 2015).

More advanced techniques attempt to address some of these problems but often bring their own demerits. Serial scanning electron microscopy (sSEM), for example, can yield images of a sample's surface using the backscattered electrons it reflects (Kuwajima et al., 2013). This is different to sTEM, that relies on electrons penetrating a sample and hitting a detector placed behind (Figure 5). A block of tissue can be automatically prepared into slices using a built-in diamond knife or focussed ion beam. The slices are then collected on a tape. Combining sSEM with this method, known as automated tape-collecting ultramicrotome (ATUM), allows samples to be scanned later and repeatedly (Baena et al., 2019). Storage on a tape in this way is compatible only with sSEM as electrons need not penetrate the tape. Another benefit is that the images derived from the slices are largely already pre-aligned, somewhat relieving computers of this task (Ohno et al., 2015).

Evidently, a significant number of person-hours can be automated by machine in this way. Many other techniques exist, all of which are relief from the meticulous work by White et al., and a step closer to data acquisition that is compatible with human connectomes (1986). sSEM has also been proposed as the necessary aide for reconstructing the entire mouse brain (Mikula et al., 2012). However, it does not overcome the issue of resolution being dependent on slice thinness, nor the destructive nature of preparing samples for scanning. Perhaps pertinent still is the invasive nature of sTEM and sSEM. They both require brain tissue that is retrieved either post-mortem or from biopsy. The latter is a procedure that poses great risk; discontinuity of the protecting skull incurs a risk of infection, haemorrhage, and other morbidities (Magaki et al., 2015; Schuette et al., 2010). Alone, this risk is enough to cement brain biopsy as the last-resort investigation for severely ill, hospitalised patients (Josephson et al., 2007), never mind healthy individuals in whom a connectome reconstruction is the goal.

2.2.2 Non-invasive: neuroimaging

For connectomics to have medical use, researchers seek to collect data in-vivo. Clearly, the field must innovate new methods that are non-invasive, pain-free, and do not depend on gross dissections. Here, we approach the heart of this study and the fringe of connectomics. At the front are two remarkable consortia who work on the “Human Connectome Project” (HCP), launched in 2009 (NIH Blueprint, 2010). They provide an open-source neuroimaging database that gives researchers access to an unprecedented number of human subjects’ brain scans. It is these efforts that enabled this paper.

The most common non-invasive method used for data acquisition in the field is MRI, owing to its safety, spatial resolution, and availability (Meoded et al., 2017). Anatomical scans, classically T1- and T2-weighted MRIs, are used to deliver high-resolution, structural information (brain shape, positions of sulci/gyri, masses etc.) and to appropriately label and segment the brain and cortex. We use other MRI

sequences to allude the connectome. It is possible, for example, to reconstruct a connectome from functional scans, such as fMRI, magnetoencephalography (MEG) and electroencephalography (EEG). However, in doing so one reconstructs the functional connectome/network, not the structural (Van Essen, Ugurbil, et al., 2012).

Therefore, a common tool for mapping the structural connectome is dwMRI. More specifically, *diffusion tensor images* (DTI), a variant of dwMRI, are used in this paper (c.f. Huisman, 2010). These work by leveraging the signals given by water protons. The protons of other molecules are also a source, but water is the dominant input in the human body given its composition. Water molecules diffuse in all directions like a drop of ink in a pool, driven by random thermal motion (Brownian motion). However, this is only true for cases where the diffusion is unbounded. Where water diffuses easier in a particular direction, we can infer surrounding structure. In this way, our analogy of ink in a pool fails. The wrapping of myelin sheaths around neurones contributes to the preferential diffusion of water along their direction. Their organisation into parallel neuronal bundles further contributes to this effect. This property, known as *anisotropic diffusion*, can be observed even in dead, non-frozen specimens (Mori & Zhang, 2006).

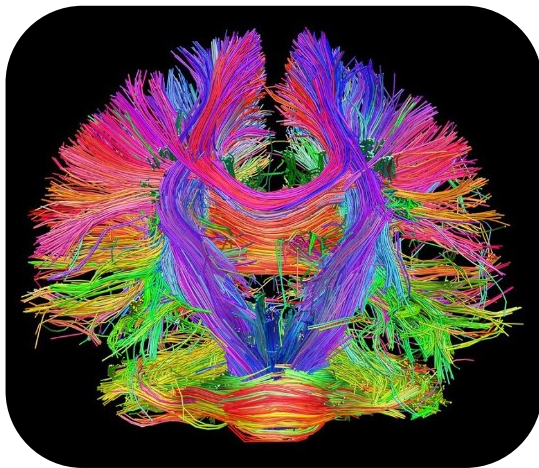


Figure 6: Frontal view of both hemispheres of a tractography-generated, structural, human connectome. Lines are neuronal fibres. A standard is applied for colouring that was suggested by Pajevic and Pierpaoli (1999), where the colour denotes fibre orientation: fibres travelling left-right are red, from anterior to posterior in green, and inferior to superior in blue. Note that directionality is lost for all colours. For example, right-left fibres are also red.

One uses this anisotropy with fibre-tracking algorithms to reconstruct the paths of neuronal bundles. Put briefly, the algorithm begins at a particular voxel (i.e., the *seed*). This voxel has a dominant direction that is determined by the directions of all the neuronal bundles it contains. The algorithm moves in this direction, advancing to the next voxel. This is repeated to form a *streamline*, that effectively traces the neuronal bundle fibres (tracts). This technique is termed *deterministic tractography* (or *streamline tractography*), and Figure 6 shows example output for one participant's whole brain. Tractography has very recently shown promise as a non-invasive prognostic tool for spinal cord injury (Costanzo et al., 2022) and for measuring axonal damage in traumatic brain injuries (Jang & Seo, 2022). It has developed

increasing interest over the last two decades and, in some countries, is now commonly used for preoperative planning of brain tumour resections (Toescu et al., 2021; Yamada et al., 2009).

2.3 THE CONNECTOME AS A NETWORK: NODES, EDGES, AND MODULES

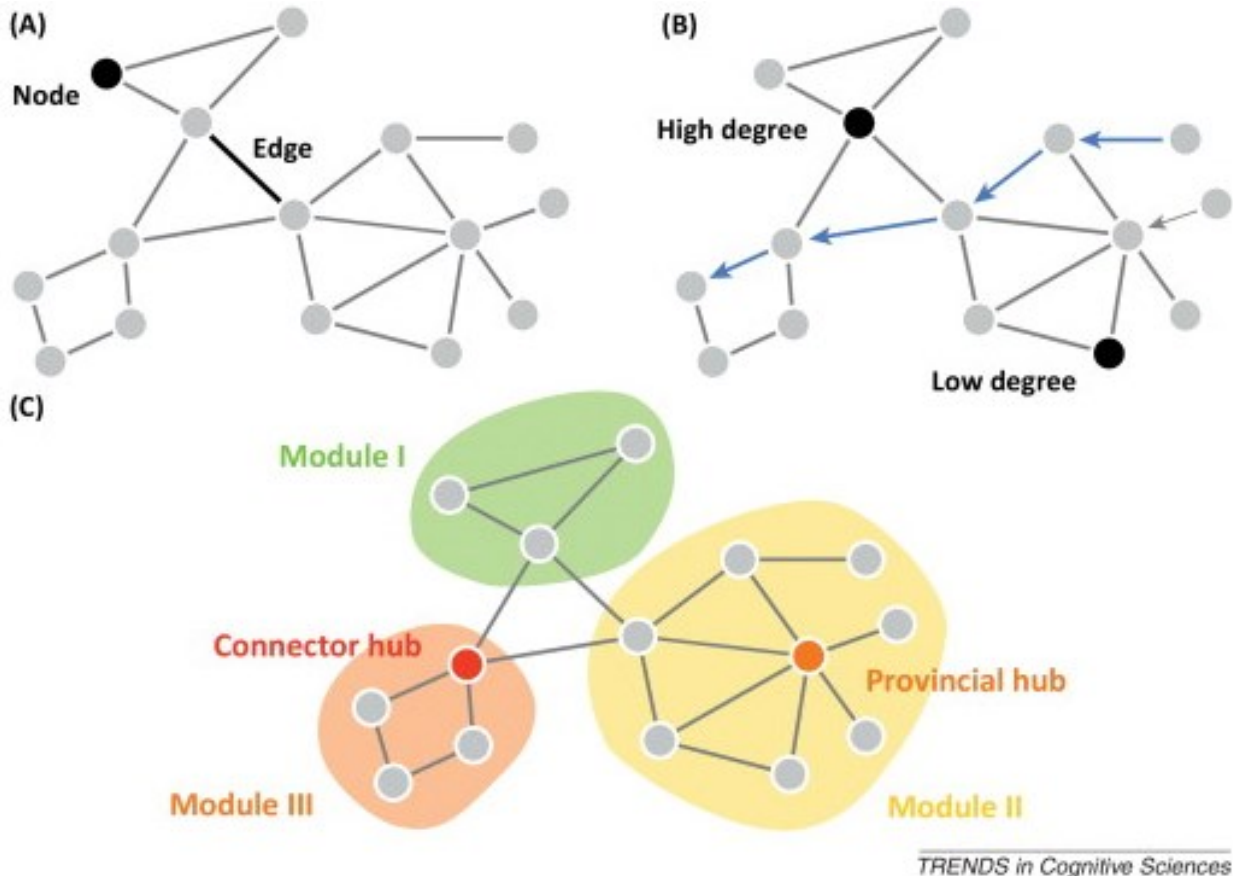


Figure 7: Basic network attributes. Reproduced from (Sporns & Van Den Heuvel, 2013).

We can interpret connectomes by representing them as a network. If we take an aerial-view map of a country with many buildings, and roads that interconnect them, we have a metaphor that describes a *network*. In our case, the buildings are sites in the brain. The roads represent neuronal projections that connect these sites. Or, using terms from the mathematical field of network theory: the buildings are *nodes*, the roads are *edges* (Figure 7). We have created a map of *network topology*. There are options for how the map is organised; where the buildings are, and how they are connected.

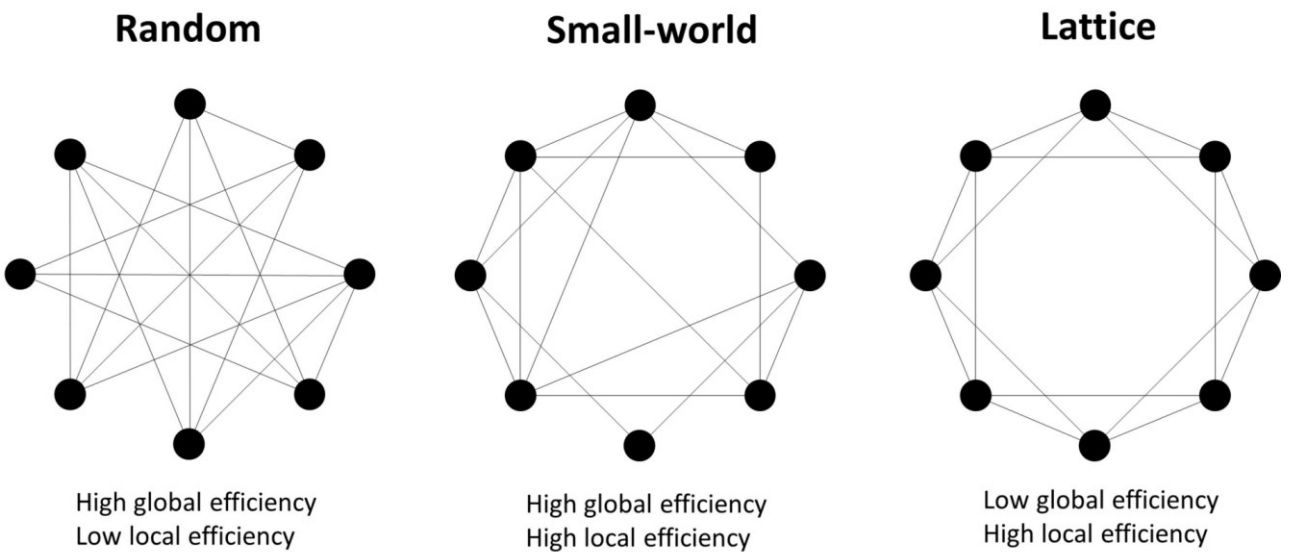


Figure 8: Examples of random, small-world and lattice network topology. Black dots represent nodes and lines are edges, or buildings and roads, respectively, if using the aerial-view analogy. Reproduced from (Zhao et al., 2015).

One option is that the map looks like a random graph (Figure 8). Roads are placed randomly so that very few are needed to travel between any two buildings (small *path length*). Anatomically, this translates to neurones exhibiting short- and long-range projections at random. This is a scenario that maximises data transfer speed, and reduces noise (Buzsaki et al., 2004). The dependence on intermediate neurones to relay a signal (i.e., a polysynaptic connection is slower than a direct (monosynaptic) connection (Bullmore & Sporns, 2012).

However, this lacks biological plausibility. One must appreciate that the greatest currency, in this context, is anatomical space. The skull's volume is finite, so it is beneficial to minimise *wiring costs* by cutting out long-range connections that occupy space, even at the expense of increasing path length. Volume constraints aside, some factors actually prevent wiring cost from being completely minimised. Neuronal somas may be displaced from their ideal position due to the presence of other structures. For the same reason, their axonal projections may also deviate from the most optimal straight-line trajectory (Bullmore & Sporns, 2012). Therefore, there must be organisation to the network.

There is a tendency for the brain's network to be modular, a notable '*small world*' property (Figure 8). This term was initially introduced by Watts and Strogatz when describing the network derived from the *C. elegans*' connectome (1998). They noted that it exhibited a high-degree of clustering but also a short path length, and remarked that this efficient topological organisation was akin to the well-known "six degrees of separation" analogy, hence "*small-world*" (Watts & Strogatz, 1998).

Similarly, human network studies have found:

- high local efficiency, or short average path length between topologically adjacent neurones (Latora & Marchiori, 2001);

- high global efficiency, as above but between non-neighbouring neurones (Achard & Bullmore, 2007);
- *modular architecture* (Meunier et al., 2009);
- and the presence of *hubs*, these are nodes that have a high number of edges (Figure 7).

These small-world characteristics develop how we should position our buildings and roads. Now, there is a need for more countries. There are plenty of roads connecting buildings within each country, but to go between countries we must traverse an inter-country connection, or flight path, and these are fewer in number than roads. Put simply, the modules of the brain are analogous to countries (Figure 7), and hubs are airports. Modules are brain areas that show dense, intra-module (local) connections. They are connected together by few long-range, hub-to-hub projections.

Remarkable evidence has found that the wiring cost of human brains is near-minimal (Cherniak, 1994). Yet, Bullmore and Sporns point out that whilst almost the case, cost control cannot be the sole driver of brain organisation. Otherwise the network would approach a regular lattice structure (Figure 8), consisting of only local connections, and many functions afforded by inter-areal communication would be lost (2012). To reason this way of organisation, neurobiologists refer to evolution and a selection for “economic wiring” (Batista-Garcia-Ramo & Fernandez-Verdecia, 2018). It is a trade-off between minimal wiring (having as few roads and flight paths as possible), and facilitation of complex brain function. A small-world topology enables brain functions to be integrated and segregated. The former describes short path lengths that aid effective exchange of data between nodes. The latter refers to modularity that, through isolation of topological areas, ensures information is handled independently between modules. This increases the capacity of the network (e.g., supports parallel information processing (Achard & Bullmore, 2007)), and the complexity of calculations that it can perform (Sporns & Zwi, 2004). Thus, cost-function balance is the goal of evolution. We investigate this balancing act, put simply as the relationship between wires and arising function.

3 METHODOLOGY

3.1 DATA ACQUISITION

An open-source dataset, *Individual Brain Charting* (IBC), that relies on adapted, HCP-inspired protocols is used (Pinho et al., 2018). 12 adults were included (10 males; 2 females; 26-40 years old, mean age 34 years old). They consented to brain scanning and did not have a psychiatric or neurological disorder. They were profiled psychometrically and otherwise screened, with exclusion criteria as follows: IQ<80 or >130; use of drugs; impaired hearing/vision; no MRI contraindication (e.g., metallic implants). These

participants were recruited by poster in France, and they received financial renumeration. (Pinho et al., 2018).

Due to incomplete data and other factors, the 12 were originally part of a group of 14; the subject IDs for those included, therefore, are listed in Appendix B alongside each participant's handedness score as per the Edinburgh Handedness Inventory (Oldfield, 1971). All participants were scanned in the following order: T1-weighted, T2-weighted, then diffusion-weighted MRIs, followed by task-fMRIs. All were collected in 2015-2016, with participants completing the task-fMRIs in a different session to the anatomical scans. No data anomalies were identified by the data collectors. A complete summary of the dataset is available in the documentation (Pinho et al., 2020). The technical specifications of the scanning equipment, and MRI sequences and parameters, are included in Appendix C. For fMRI data, we use the anterior-posterior phase-encoded files.

3.1.1 Functional task MRI (task-fMRI)

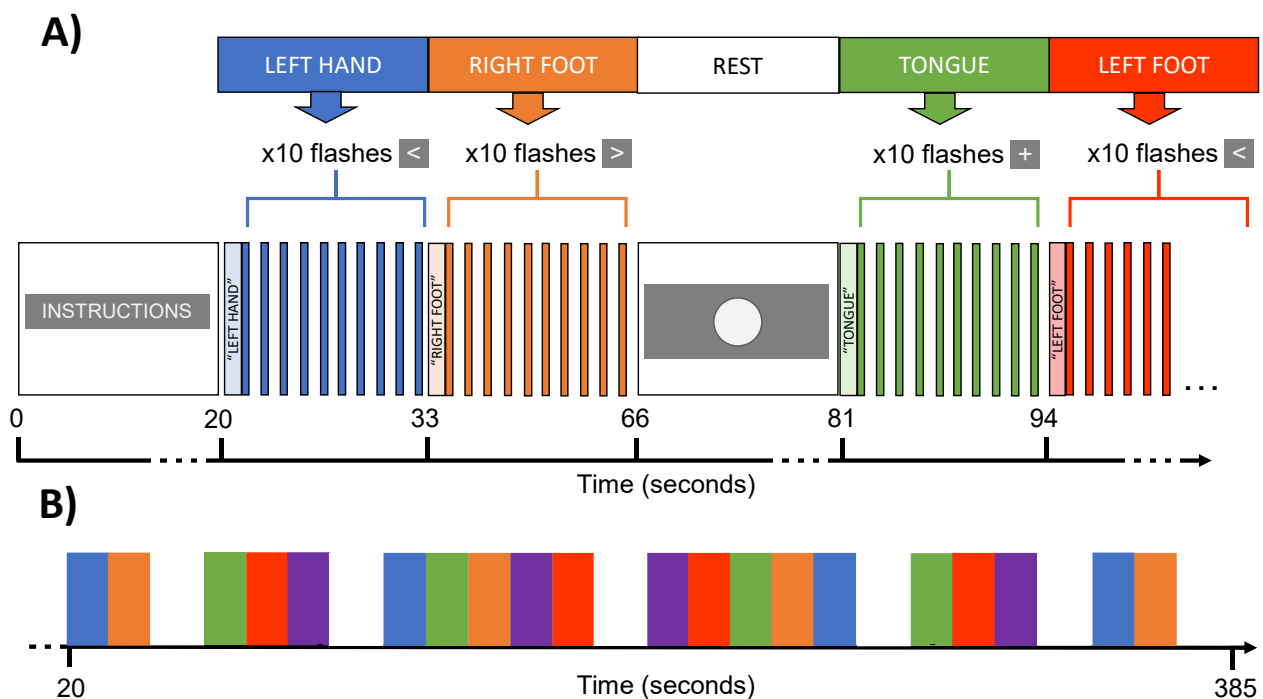


Figure 9: A) Schematic showing first 1 minute 30 seconds (approximately) of block-design experiment. Five block categories were used: left hand, right hand, left foot, right foot, and tongue. Blocks were pseudo-randomised but fixed for all participants, and each block began with a 1-second cue (e.g., "left hand"). For the following 12 seconds, movement was prompted by an arrow/cross that flashed on the screen ten times at a constant interval. Thus, each block lasted 13 seconds and contained 10 trials. Between some blocks, a fixation-dot period of 15 seconds was shown, where participants were instructed to rest. B) Schematic showing block order of block-design experiment. Blue boxes represent the left-hand category, orange are right foot, white are rest, green are tongue, red are left foot, and purple are right hand. Each block category was shown four times, and the rest block shown 7 times, leading to 27 blocks shown to each participant. With the initial instruction screen on show for 20 seconds, the total experiment took 6 minutes 25 seconds per participant.

The task-fMRIs were collected by block-design experiment, chosen over event-related paradigms because of their improved statistical rigor, or optimal detection power (Aguirre, 2011). As shown in Figure 9,

participants were primed for 1-second. For instance, “Left Hand” was displayed on-screen. Then, they were to tap this body part in time with the flashing arrow/cross. The direction of the arrow was a reminder of which side of the body to move (e.g., left-pointing arrow for left hand). A cross was flashed for blocks of tongue movement. For this block, participants were instructed to move their tongue side-to-side, with no preference of which side to start from. The images given to participants explaining the desired movements are in Figure 10. The technical validation of these fMRI data are discussed by Pinho et al. (2018).

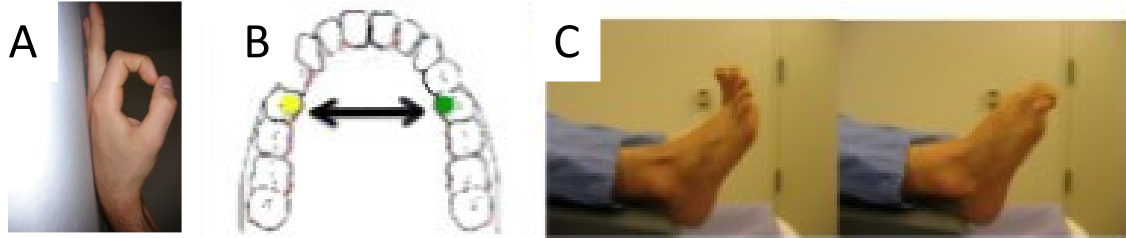


Figure 10: Images shown to participants to instruct desired bodily “tapping” movements. A) pincer-grasp movements, repeated alternation between complete relaxation of the hand and bringing together of the index finger and thumb (of indicated hand). B) alternating extension-relaxation of toes (of indicated foot), and C) side-to-side movements of the tongue.

3.2 DATA PROCESSING

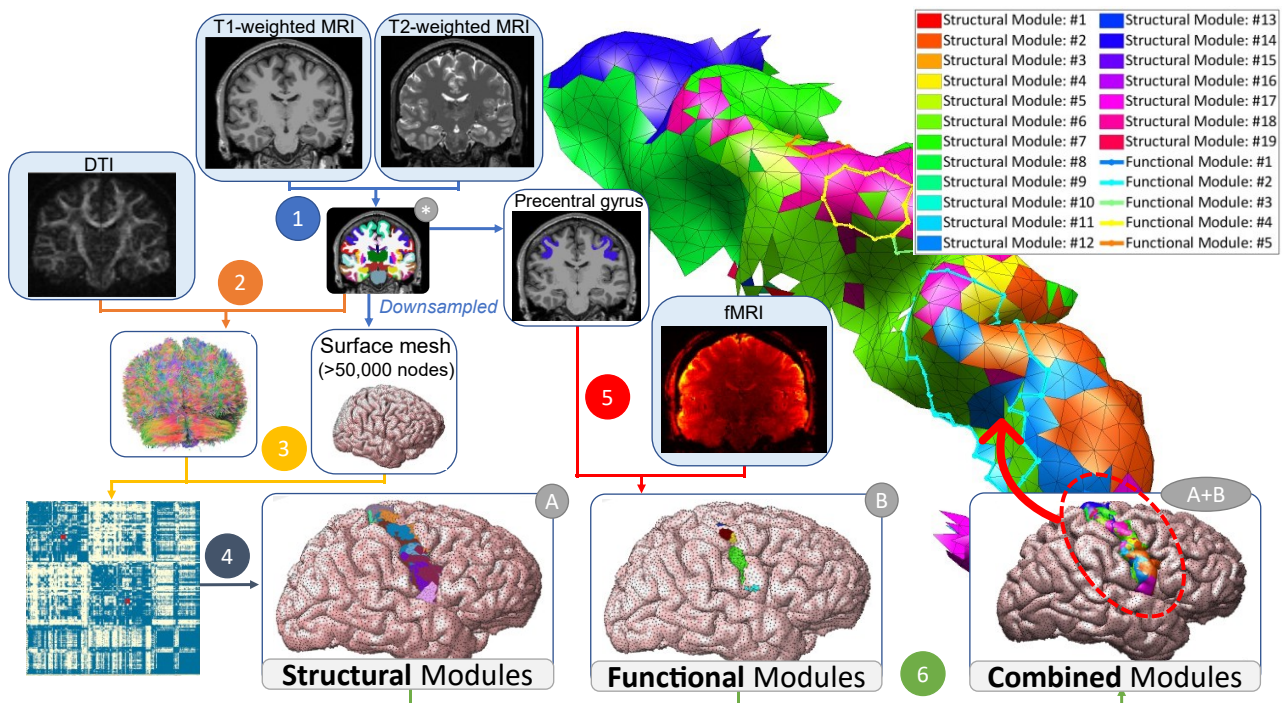


Figure 11: Methodology summary. A single subject’s pipeline (ID: 01) for a single condition (tongue movement) is shown. Scans laid upon a blue background are unprocessed data. These are processed (and sometimes combined with other data) as represented by a straight/right-angled arrow. The brain scan marked with an asterisk is the “aparc+aseg” volume, that has been labelled and parcellated by FreeSurfer. At the end of the pipeline (marked A+B) is the right hemisphere, with the precentral gyrus’ structural (shaded) and functional (outlined) module groups superimposed. A magnified view of this is shown at the end of the red

curved arrow. Note that colours of modules are inconsistent between A and B, and A+B, to aid visualisation. Therefore, the legend (top right) is applicable only to A+B and magnified views.

fMRI data are processed and compared against DTI. Figure 11 summarises this procedure, ultimately mapping the structural and functional modules in the same space. Then, we calculate spatial overlap of the two sets. We describe in detail how both maps are computed, but immediately note that *functional modules* are simply clusters of activation captured by fMRI; there is no calculation of underlying functional/effective connectivity, as would be seen with analyses of resting-state fMRIs, for example (Shahhosseini & Miranda, 2022). Despite this, we persist with the term “functional module”, over phrases like “clusters of activation”, for simplicity. Furthermore, we avoid normalising the brain, but we ensure the data are in the same anatomical space for each participant. This was verified manually at each stage using FreeSurfer’s Freeview software (<https://surfer.nmr.mgh.harvard.edu/fswiki/FreeviewGuide>).

3.2.1 Finding and defining structural modules

To define structural modules, the workflow largely follows that of Taylor et al. (2017). However, some changes were made to maintain compatibility with present day software and to facilitate parallel processing. The GitHub changelog is can be consulted for further inspection (Hill, 2022).

First, the anatomical scans undergo cortical surface reconstruction and volumetric segmentation (Figure 11, step 1). This is performed by Freesurfer, an image analysis suite (<http://surfer.nmr.mgh.harvard.edu/>). Its output is extensive but includes pial surface files and volumes with gyral-based labels as per the Desikan-Killiany atlas (Desikan et al., 2006). We use these labels, such as precentral gyrus (Figure 11), to filter/mask regions for intra-areal study. Freesurfer additionally performs motion correction, removal of non-brain tissue and intensity normalisation. Afterwards, the pial surfaces are also downsampled from >650,000 nodes to >50,000 (Figure 11 and Figure 3) using the MATLAB software package, Iso2Mesh (Qianqian & Boas, 2009).

The DTI data are inputted to a separate software package, DSI Studio (Fang-Cheng, 2007), for deterministic tractography (Figure 11, step 2). The whole brain is seeded, and generalised q-sampling imaging is performed with a diffusion sampling length ratio of 1.25. The end of a tract is determined when the terminal voxel of its streamline is less than Otsu’s threshold (0.6). Unlike Taylor et al., who collated ten runs of 1-million fibres at random, we collected 10-million fibres in a single run. This improvement is likely small given the randomness of seeding but is nevertheless optimal. Parameters were mostly unchanged and chosen according to previous work (Yeh et al., 2010): step size=0.625mm; smoothing=0; seed orientation=“primary”; seed position=“subvoxel”; tracking algorithm=“Streamline (Euler)”. Some parameters were constrained to enforce biological plausibility. Only streamlines of length 10-300mm (inclusive) were permitted, and those with sharp turning angles (>60 degrees) were also discarded. Upon completion of this step, we yield a representation of the structural connectome. Using DSI Studio’s built-

in co-registration abilities, we co-register the connectome with the parcellated, segmented brain volume, “aparc+aseg” (Figure 11). The exact algorithm used for this is not publicly available.

Next, we convert the output into a high-resolution connectivity matrix (Figure 11, step 3). Previous studies generate a matrix using only streamlines that do not have endpoints terminating in white matter (Taylor et al., 2017). To conform to this standard, we ensure all endpoints terminate in either the grey matter or subcortical areas defined in “aparc+aseg”. For each streamline, we then take its endpoints and find their nearest nodes (Euclidian distance) on the parcellated surface mesh. The endpoints are then used to build a binary connectivity matrix (Figure 12).

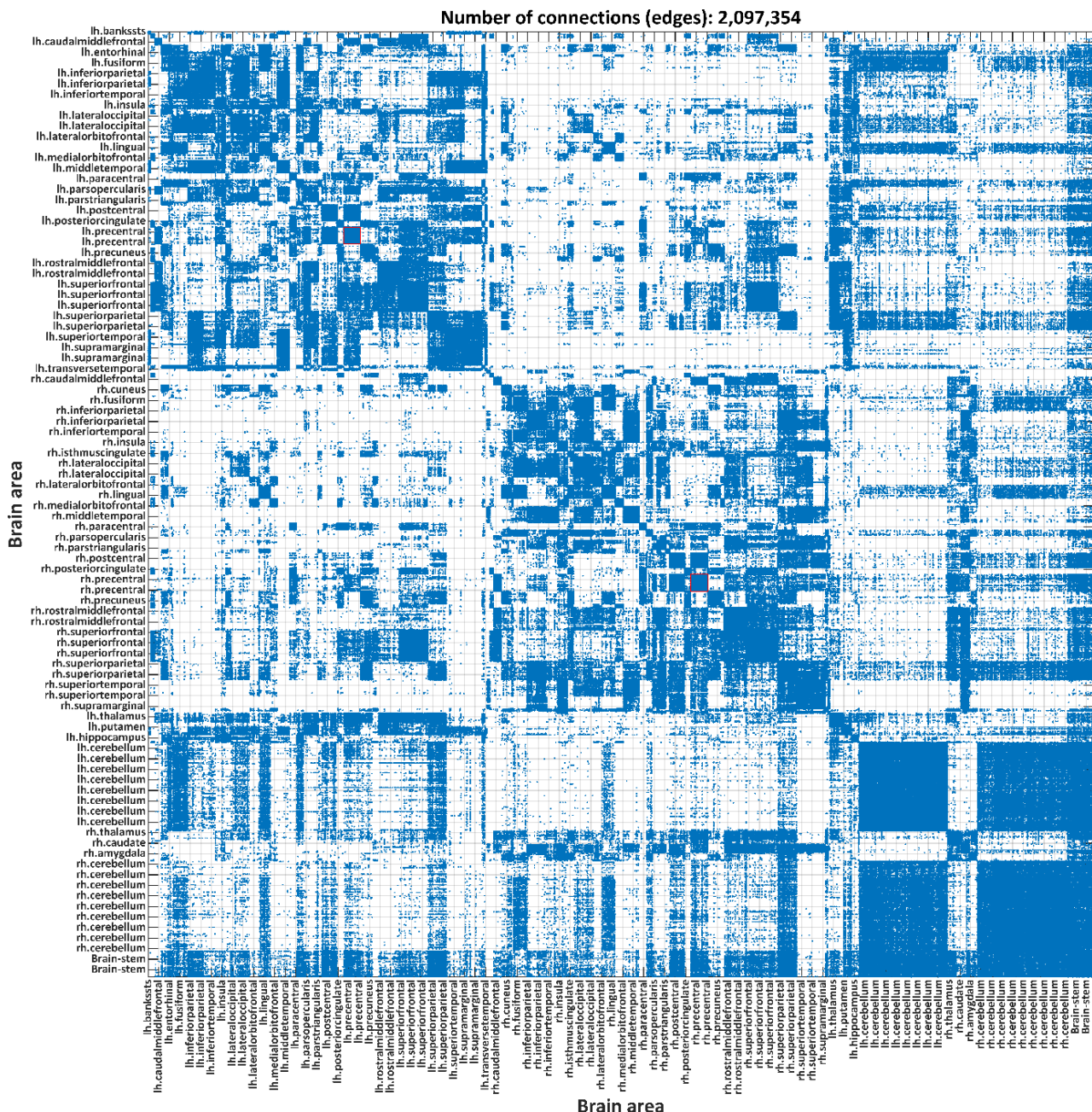


Figure 12: High-resolution global connectivity matrix of a single subject's (ID: 01) cortical and sub-cortical brain regions. More than 2 million connections are shown. The connection between two nodes is shown by a blue dot, and the brain areas' labels are indicated by the axes. Note that due to varying size, some area

labels are omitted, and some are duplicated. The brain area labels are formatted as per FreeSurfer's lookup table (<https://surfer.nmr.mgh.harvard.edu/fswiki/FsTutorial/AnatomicalROI/FreeSurferColorLUT>). For example, a prefix of "lh.-" indicates a left hemispheric region. When combined with "-precentral", the label describes the precentral gyrus of the left hemisphere. The intra-areal connections of this region, and its right-hemisphere counterpart, are indicated by red-bordered boxes. This figure is accompanied by further figures of magnified, selected regions (see Appendix D).

We independently select the precentral gyri from the global connectivity matrix. We use MATLAB's Brain Connectivity Toolbox, written by Rubinov and Sporns (2010), to find modularity within gyri. Specifically, we apply the toolbox's Louvain community-detection algorithm (first outlined by Blondel et al. (2008)) to the local connectivity matrices. For each participant, the optimal γ was found by scanning the parameter space in increments of 0.02 from 0.6-1.4 (inclusive). The modularity score for the dataset at each γ value ($Q_{CORTICAL}$) was compared against the same score from a random network of the same number of nodes and edges (Q_{RANDOM}). We repeated both calculations 25 times, and mean scores were calculated:

$$\bar{Q}_{CORTICAL} = \frac{1}{25} \sum_{i=1}^{25} Q_i^{CORTICAL}$$

$$\bar{Q}_{RANDOM} = \frac{1}{25} \sum_{i=1}^{25} Q_i^{RANDOM},$$

Equation: 1

such that the optimal γ yielded the highest Q_{MAX} ,

$$Q_{MAX} = \bar{Q}_{CORTICAL} - \bar{Q}_{RANDOM}.$$

Equation: 2

In other words, the chosen γ consistently gave the greatest number of modules, relative to random networks. It is possible to visualise network topography after module assignment (e.g., Figure 13 is an example of Figure 7 placed in context). Additionally, modules can be shown in anatomical space by colouring faces of the brain surface mesh (Figure 14). The graphics of this type were subsequently delivered by the "plotsurf/plotedge" functions of the same Iso2Mesh package used for downsampling.

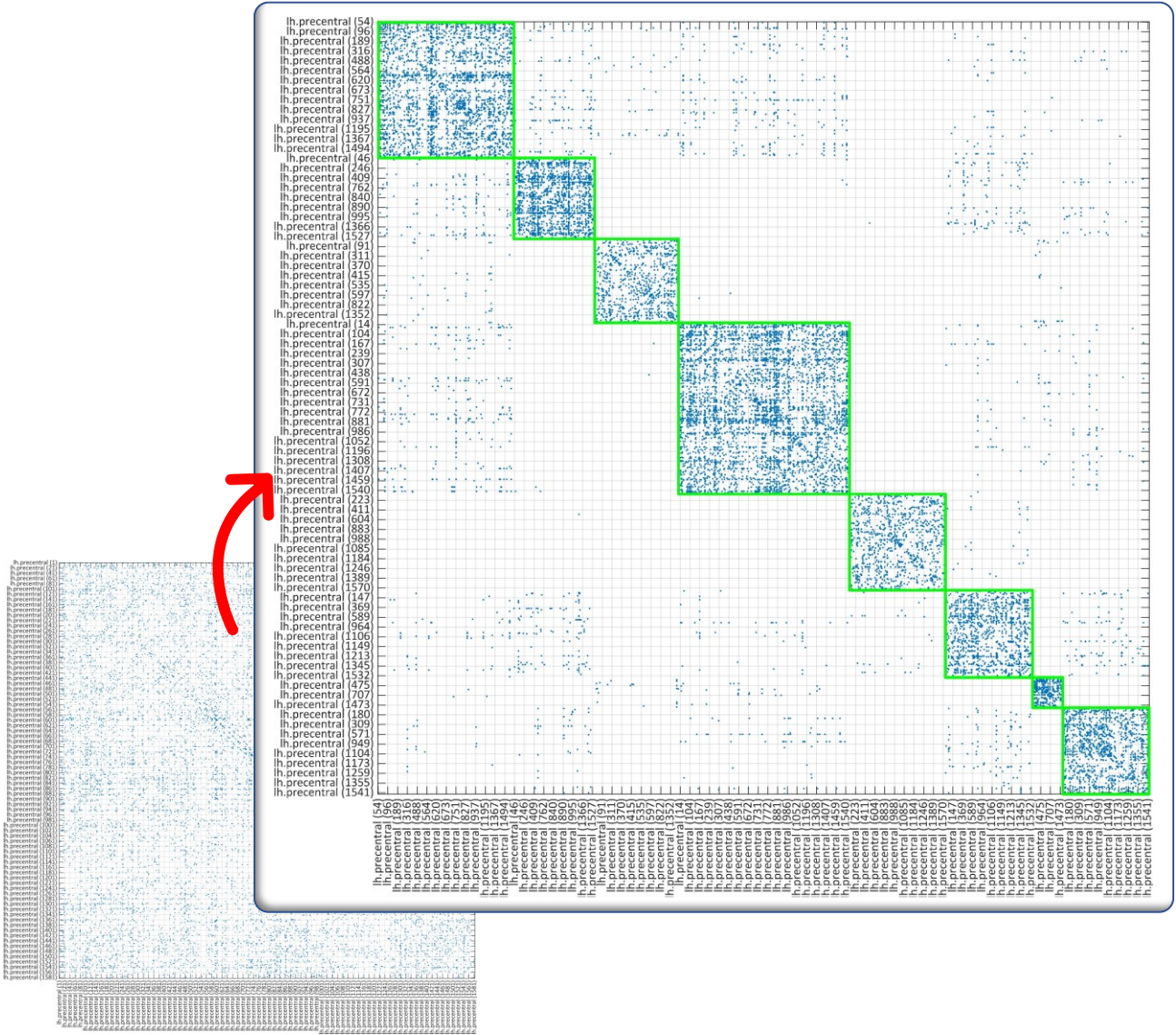


Figure 13: Reordered local connectivity matrix of a single subject's (ID: 01) left precentral gyrus to show module assignment. Bottom left shows the original local connectivity matrix (see: Figure 26). Following the application of the Louvain algorithm, one can reorder the nodes on the map so that topological (network) neighbours are adjacent. This reveals the top-right image, showing repositioned nodes (refer to axes numbering) within the left precentral gyrus. Green squares indicate module assignment. One module exists in the upper-left corner but, due to being too small, is difficult to observe for counting. Nine structural modules are found.

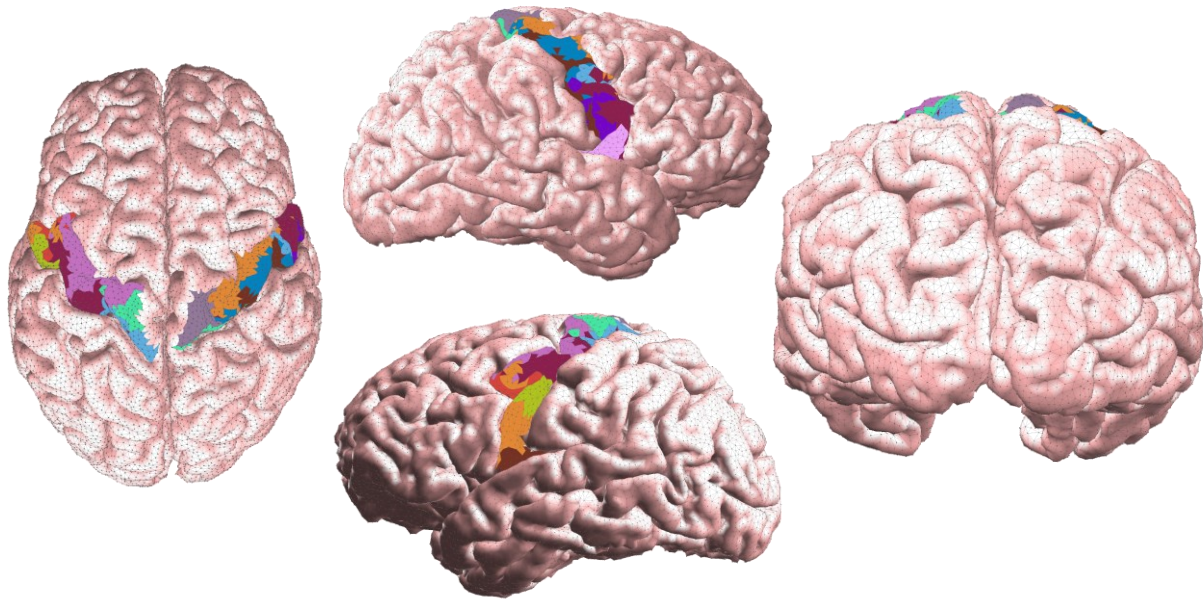


Figure 14: Structural modules of a single participant’s (ID: 01) precentral gyri. All images show the resampled (>50,000 node) brain surface. Colours on the precentral gyri indicate module groups of the nodes (triangular faces). The modules on the left hemisphere are independent of those on the right. Left – superior view. Middle column – lateral views. Right – posterior view.

3.2.2 Finding and defining functional modules

Functional modules are task dependent. Consequently, the following actions were applied for each participant’s motor task (to “task-HcpMotor_acq-ap_bold.nii” files):

1. Time-series realignment and reslicing,
2. Slice timing correction,
3. Co-registration,
4. Smoothing,
5. Modelling and result reporting,
6. fMRI to brain surface mapping.

Statistical Parametric Mapping (SPM12, <https://www.fil.ion.ucl.ac.uk/spm/>) software was used for actions 1-5, and custom MATLAB scripts thereafter. The analysis of the functional neuroimages was guided by the preprocessing pipeline outlined in Andy’s Brain Book (Jahn, 2022). Some parameters were changed from SPM defaults in accordance with best practice.

3.2.2.1 Time-series realignment and reslicing

The fMRI data are first realigned and resliced for each subject using a least-squares approach and a 6-parameter (rigid body) transformation (Friston et al., 1995). This motion correction accounts for fluctuations in pitch, roll and yaw of the head that naturally occur during scanning. All volumes are aligned to a mean image using a 2-pass procedure: first pass aligns the volumes, second pass reslices them to a

mean image calculated from all volumes. The remaining parameters follow the defaults proposed by SPM12.

3.2.2.2 *Slice-timing correction*

Given that the fMRI protocol used a long repetition time (TR=2seconds), we must also correct for the fact that volume slices were not collected simultaneously. Such slice-timing correction is especially pertinent here owing to the positioning of the precentral gyri. Evidence has found this approach to significantly increase statistical power for dorsal brain regions (Sladky et al., 2011). Consequently, the realigned slices from the previous step undergo slice-timing correction. This is a method of interpolation that uses a reference slice obtained at time zero ($t=0$ milliseconds) and adds lag to the data as if each slice were obtained at the same time.

3.2.2.3 *Co-registration*

Here, the T1-weighted anatomical scan is incorporated, as ensuring that all scans are in the same space is crucial to this work. Already, the structural connectome (DTI-derived) was co-registered to the T1-weighted scan. Therefore, the same procedure follows for fMRI. We take the mean fMRI image calculated during time-series realignment (i.e., the source image) and move it over the anatomical scan (i.e., reference/target image) until the best alignment of the two is found. This is termed a rigid-body model and, mathematically, is performed using SPM12's in-built Powell optimisation algorithm that uses normalised mutual information.

To reduce the chance of finding local minima, the anatomical scan is first duplicated, and the origin of the copy is redefined as the anterior commissure (AC). This is repeated for the functional scan. Then, a transformation matrix is calculated by Freesurfer's "tkregister2" function to allow conversion between the old anatomical set (default origin) and new (AC origin). In this way, the previous T1-DTI co-registration is unaffected, and the likelihood of this co-registration's success is maximised. Lastly, we use Freesurfer's Freeviewer tool and MATLAB plots to confirm the appropriate co-registration of DTI, T1-weighted MRI, and f-MRI for each participant.

3.2.2.4 *Smoothing*

The fMRI data is smoothed to help improve signal-to-noise ratio, where signal is defined as the data we want to measure, and noise is any additional data (often secondary to "system-related instabilities, subject motion, and physiological fluctuations" (Liu, 2016)). Smoothing replaces each voxel's value with the mean of its neighbours. We apply SPM12's smoothing function to our fMRI data, changing the default full-width at half maximum parameter from 8mm to 5mm (Pinho et al., 2021).

3.2.2.5 Modelling and first-level analysis reporting

SPM12 applies a mass-univariate approach based on the general linear model (GLM) to the fMRI data. That is, the program assumes that the fMRI data (dependent variable, Y) are the result of a weighted combination of explanatory variables (X):

$$Y = \beta_1 X_1 + \beta_2 X_2 \dots + \beta_N X_N + \varepsilon$$

Equation: 3

We add weights to the sum using β (or parameter estimates), and ε represents the residual (Jahn, 2022).

By adjusting β , one can propose how much the explanatory variable, or motor task, modulated the fMRI signal. A simple overview of GLM is that it attempts to fit the acquired fMRI data to a model.

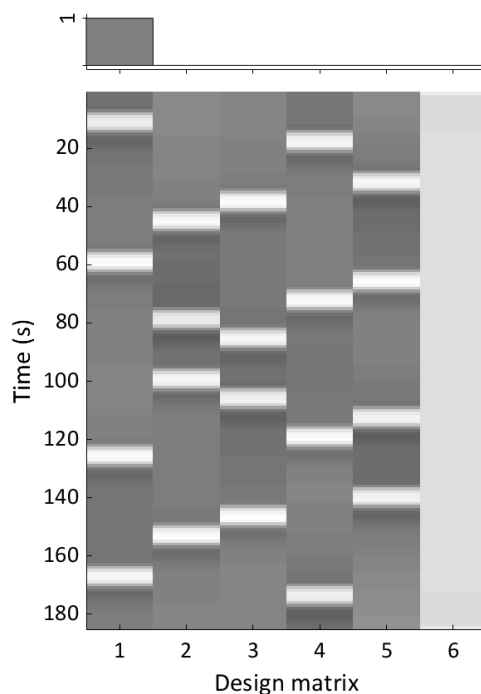


Figure 15: Top – The contrast used in SPM12 for the “left hand” motor task. Columns are implied by the design matrix beneath. Bottom - design matrix of the GLM. Lighter colours represent greater proposed brain activity. Y-axis displays increasing scanning time (seconds) as you descend each column. Columns, from left to right, are ideal time-series for: 1) left hand movement, 2) right hand movement, 3) left foot movement, 4) right foot movements, 5) tongue movement, and 6) mean signal of the scanning session (baseline).

We first propose and estimate the model using a design matrix from 5 explanatory variables (for each of the motor tasks) and timing files that depict when each task was performed (Figure 15, bottom). By finding the difference between β for all voxels across the time-series, SPM12 yields a voxel-wise contrast map. This can be interrogated to find voxels (statistical parametric maps) that were modulated by each task using t-contrast vectors. For instance, a contrast of “+1 for left hand, 0 for other tasks” (Figure 15, top) indicates a preference for voxels that were sufficiently activated by movement of the left hand but showed no change in activity for other tasks. This is in comparison to “+1 for left hand, -1 for other tasks”, which would select voxels activated by left hand movement but elicit a deactivated (below-baseline) response

for other movements. Given this work’s inquisition, we opt for the former contrast, set-up for all tasks. We also mask the results to calculate only precentral gyri voxels (Figure 11, step 5). Activations may contain any number of voxels, provided they are significant (extent (k) = 0; $p_{FWE} < 0.05$ (cluster-corrected)). The outputted binary volume is exported (Figure 16).

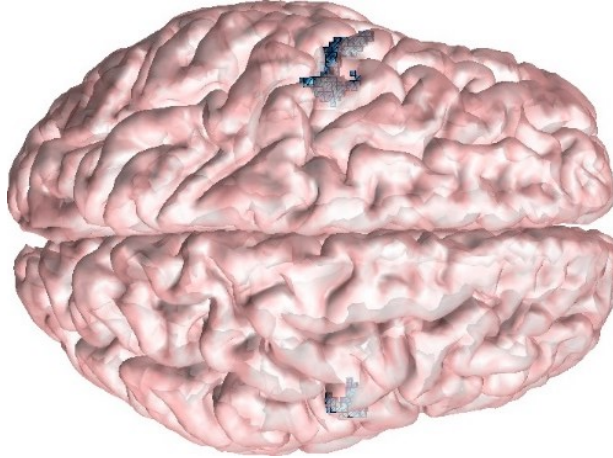


Figure 16: The output from SPM’s GLM (participant: sub-01; motor-task: tongue) is a binary volume, where its ‘on’ voxels indicate fMRI activation. These are shown here as blue voxels embedded within the brain of a single participant (ID: 01). Note that they may reside deeper in, away from the cortical surface.

3.2.2.6 fMRI to brain surface mapping

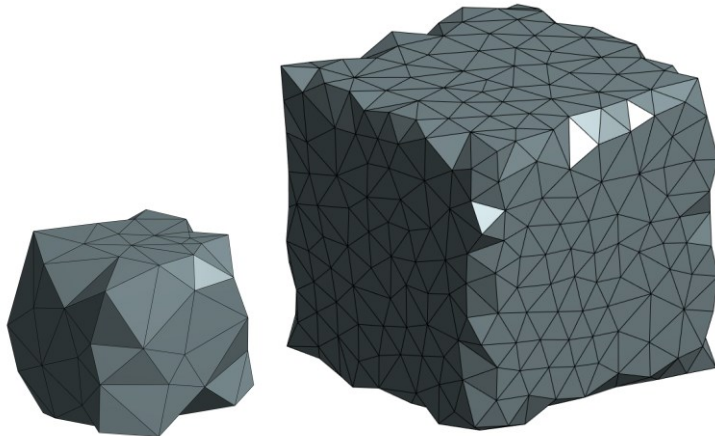


Figure 17: Left – A 2-by-2-by-2 cube (arbitrary units) as processed by ISO2Mesh’s “vol2surf” function. Right - A 100-by-100-by-100 cube (arbitrary units) as processed by ISO2Mesh’s “vol2surf” function. Both - Rather than finding the surface of a perfect cube, the nature of the task means the resulting surface is deformed. As the size of the object increases, the ability for the function to correctly match the desired surface improves.

The final step to defining the functional modules is the projection of task-activated voxels to the cortical surface. They are first grouped into modules by their spatial location using MATLAB’s “bwlabeln” function. Voxels with touching faces or edges (but not vertices), in any direction, are considered a unitary module and its surface is computed. After which, this surface is projected onto the surface of the cortex. This step is performed by calculation of mean Euclidian distance between the vertices of each module surface to the left/right cortex, and the smallest mean distance (i.e., should a module be projected to the left or right hemisphere?) is chosen. Iso2Mesh’s “dist2surf” provides the cortical surface vertices to which

the module is closest, and the module's vertices are then independently projected to their nearest surface vertex on the specified hemisphere's precentral gyrus.

All projections were completed successfully. Given an fMRI resolution of 1.5mm cubic voxels (with 5mm smoothing applied), and the inaccuracies caused by dividing this isometric cube's surface into non-standardised triangles (Figure 17), modules were reasonably close to their nearest cortical nodes (Figure 18). Following their projection, the same principles for structural modules were applied to visualise the functional modules in anatomical space (Figure 19).

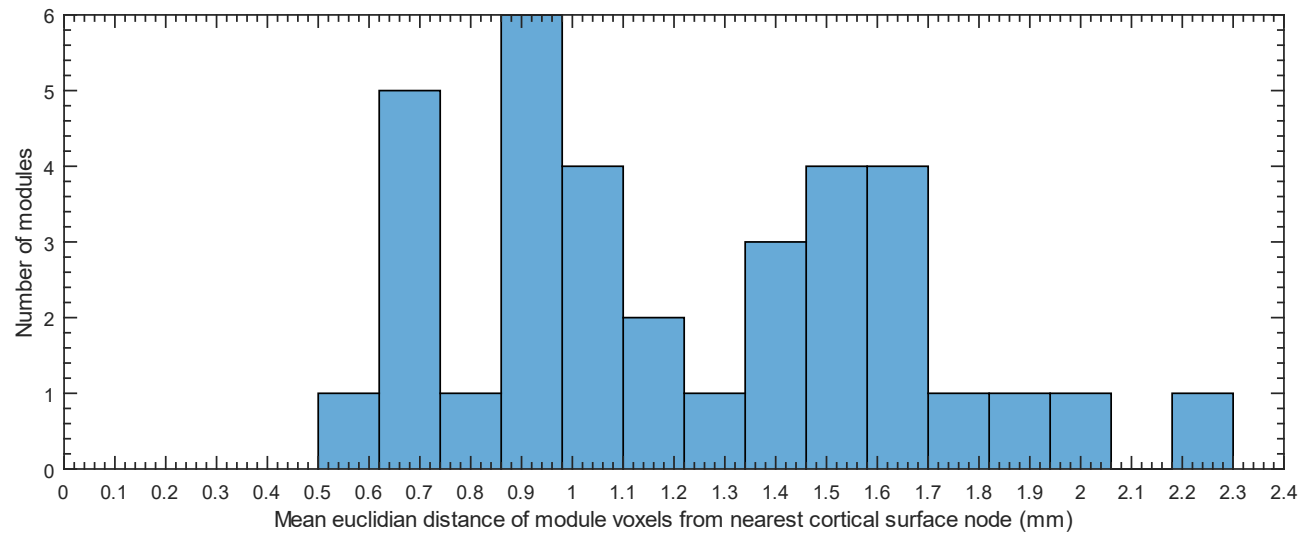


Figure 18: Histogram showing the mean distances of modules' voxels from their nearest cortical surface node for all participants. Minimum distance=0.5927mm, maximum=2.2999mm, and mean=1.2247mm.

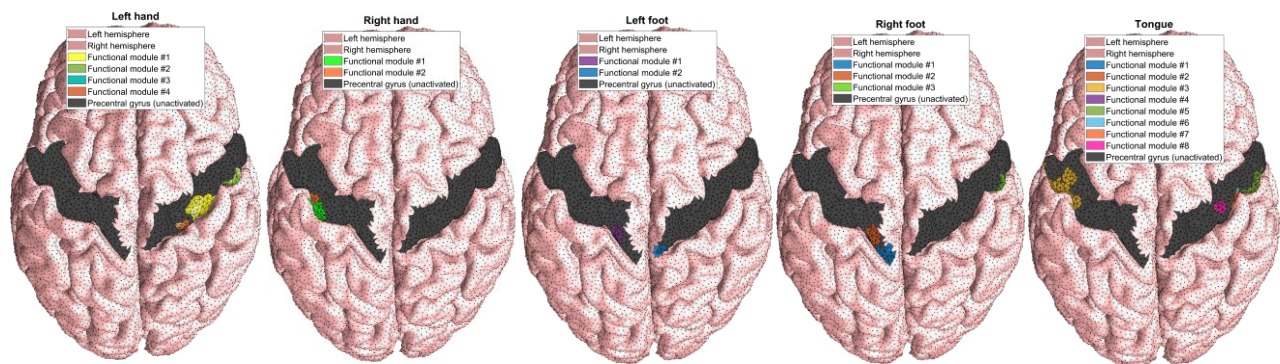


Figure 19: Functional modules of a single participant's (ID: 01) precentral gyri. All images show the resampled (>50,000 node) brain surface. Colours on the precentral gyri indicate module groups of the nodes (triangular faces). The modules on the left hemispheres are independent of those on the right. Similarly, modules vary between motor tasks. Motor tasks are, in left-right order: left-hand, right-hand, left-foot, right-foot, tongue.

The two module sets are compared in anatomical space (Figure 11, step 6). The meshed surface of the brain, with its >50,000 triangular faces, serves as the template for labelling. Two module labels (e.g., "structural module number: #3", "functional module number: #1") are applied to the faces of the precentral gyri. The size properties (absolute and relative surface area in millimetres) of functional module(s) are compared against their underlying structural module(s).

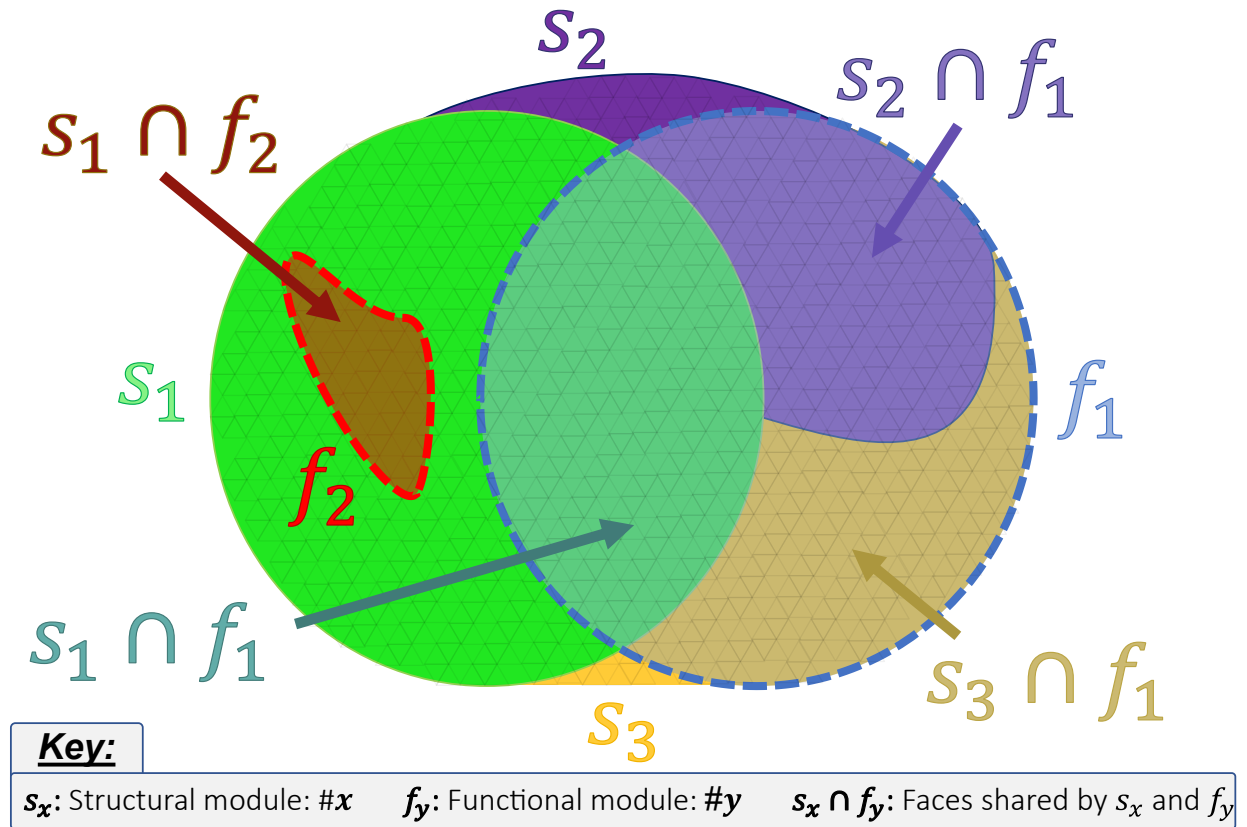


Figure 20: A schematic of a portion of the precentral gyrus surface. Faint triangular faces represent the nodes of the downsampled cortical surface (as seen in Figure 3). Three structural modules are shown (S_1, S_2, S_3), and two functional modules are superimposed (f_1, f_2), bordered by a dashed line. The overlap between the sets is displayed and labelled using \cap . Note that in our simulations (see Appendix E, module shapes are bound to the vertices of triangular faces (not shown here due to simplification); thus, partial coverage of a triangle by either s_x or f_y does not occur.

Figure 20 assumes a modified Venn diagrammatic problem where each set (s_x and f_y) takes the module's shape and size, as determined by its constituent triangular faces. Faces of structural module, s_x , may also have functional module, f_y , represented by an area of overlap (e.g., $s_x \cap f_y$). Modules of the same type do not overlap (i.e., s_x and $s_{x'}$ are mutually exclusive). Structural modules do not change between motor tasks, unlike functional modules.

$$\text{Mean overlap (mm)} = \frac{(s_1 \cap f_2) + (s_1 \cap f_1) + (s_2 \cap f_1) + (s_3 \cap f_1)}{4}$$

Equation: 4

Figure 20 highlights that more than one functional module may exist, and each may be specific to one structural module (i.e., f_2) or diffused across many (i.e., f_1). Therefore, to simply investigate structure-function overlap as the mean area of all intersections would be unhelpful (Equation: 4) as module-specificity would be lost. Furthermore, it would be affected by functional module size (the larger the functional module, the larger any intersection). Given that different motor tasks are processed by variably sized cortical surfaces (Figure 1), this would further confound results with a task dependency. Lastly, the existence of more than one functional module, perhaps one large and some smaller, may be secondary to

non-event-related brain activations (e.g., noise, incorrect). For all reasons described, we therefore seek to identify the most pertinent functional module per motor task and normalise its overlaps. We also acknowledge that the boundaries of functional modules will be affected by our methodology (e.g., projection to surface inaccuracies (Figure 18)), such that mild non-specific behaviour ought to be weighted less. Thus, we present the following solution:

1. For every intersection, we calculate its relative cover of the underlying structural module,

$$i_{(x,y)} (\%) = \frac{(s_x \cap f_y)}{s_x},$$

Equation: 5

2. A functional module is selected, (f_*), that has the largest i . (Other f_y are ignored.)
3. The mean of all non-zero areas of intersections of f_* and its underlying structural modules, weighted by the size of the intersection relative to the functional module's, is calculated, and reported as the optimised overlap,

$$\bar{i} (\%) = \frac{\sum_{x=0}^n [i_{(x,*)} (s_x \cap f_*) \frac{1}{f_*}]}{\sum_{x=0}^n (s_x \cap f_*) \frac{1}{f_*}}, \quad \text{where } (s_x \cap f_*) > 0$$

Equation: 6

We include some results (e.g., Figure 24) that presents normalised overlap from all intersections (i.e., non-optimised). For these, Equation: 6 can be advertently modified to replace instances of f_* with f_y .

4 RESULTS

4.1 LARGER FUNCTIONAL MODULES ARISE FROM MORE STRUCTURAL MODULES

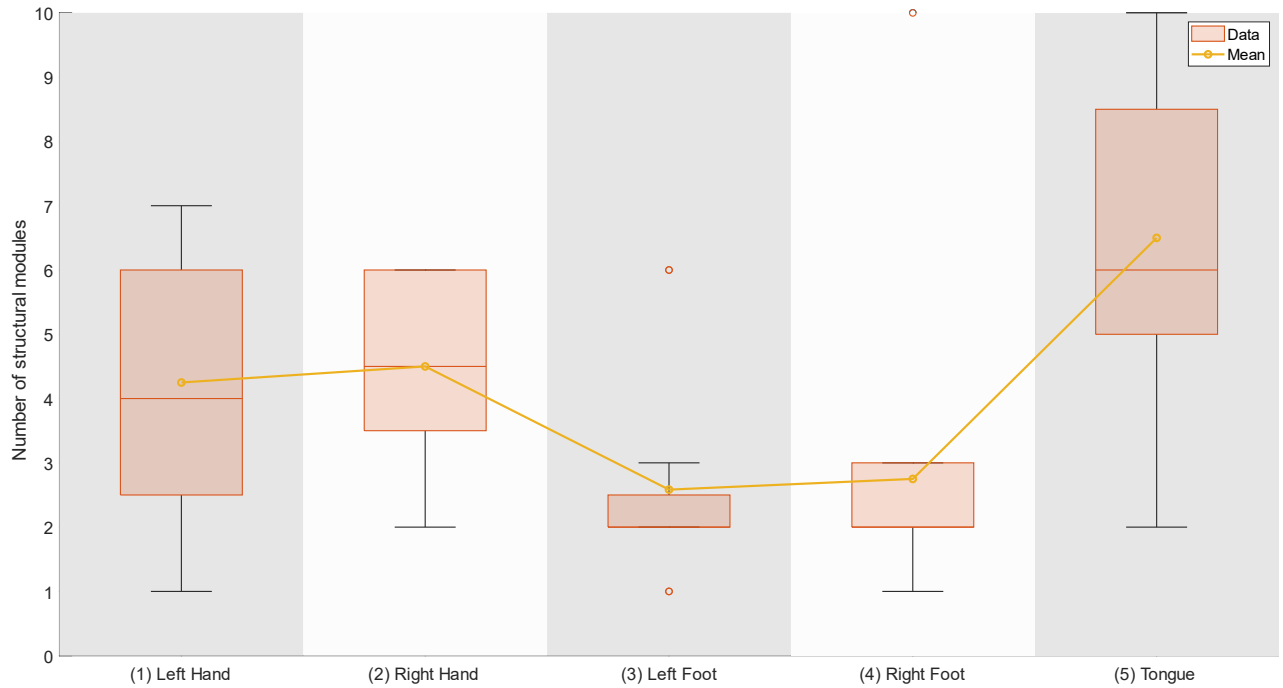


Figure 21: Distribution of number of structural modules per f_ by motor task. Data for all subjects ($n=12$) included. Only for 5 out of the 60 participant and motor task combinations is f_* encapsulated by a single s_x : sub-06 and left-hand; sub-02, sub-13 and left-foot; sub-09, sub-14 and right-foot. Thus, >90% of the functional modules (f_*) measured, despite our selection for the optimal, overlapped with numerous structural modules. The same figure, but using non-optimised data (f_y), is also available (see Appendix F).*

In Figure 21, it is observed that functional modules typically arise from more than one structural module and the quantity is dependent on the motor task but independent of side of body (mean number of structural modules: left hand=4.25; right hand=4.5; left foot=2.6; right foot=2.8; tongue=6.5). It appears that the number of activated structural modules scales with increasing size of the motor homunculus region. For example, we see that the large motor homunculus area responsible for tongue movement, corresponds to a larger number of recruited structural modules. Fewer are recruited for smaller homunculus areas.

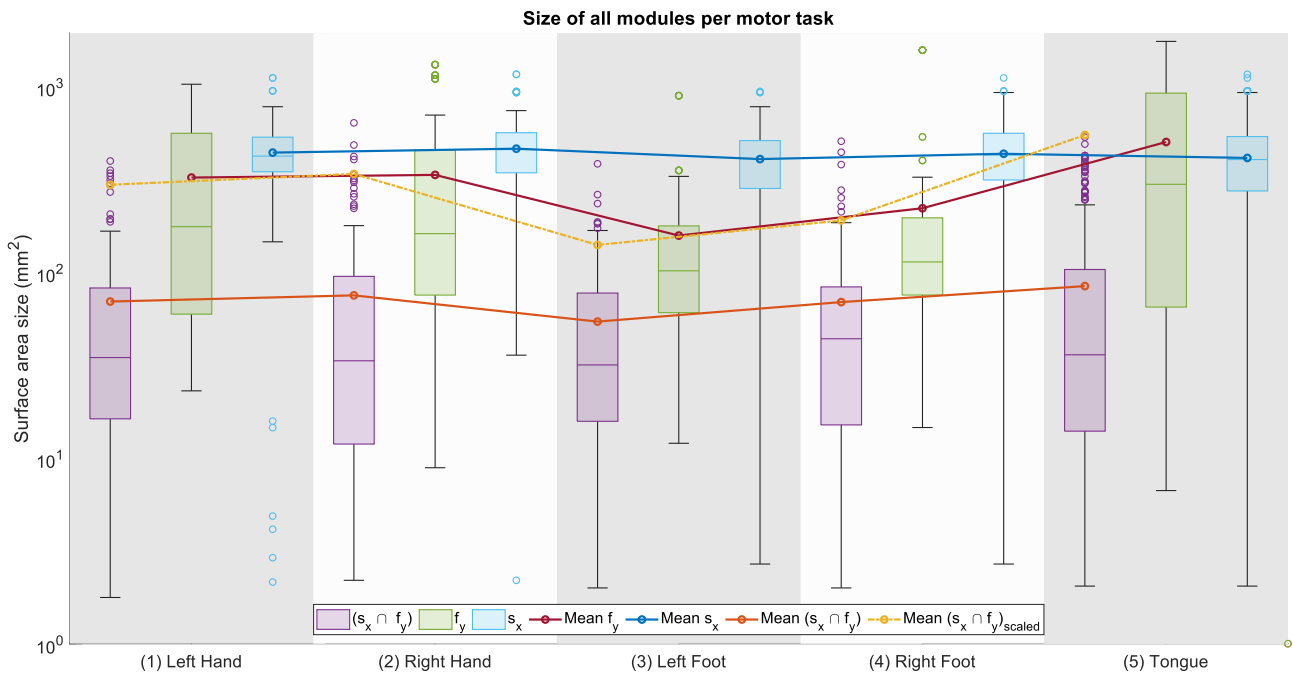


Figure 22: Boxplot showing surface area size in squared millimetres of $(s_x \cap f_y)$, f_y and s_x , respectively, for all motor tasks. The means for all surfaces are also plotted. Mean $(s_x \cap f_y)_{\text{scaled}} = \text{mean number of structural modules per task multiplied by their average size (Mean } (s_x \cap f_y))$. Data for all subjects (n=12) included. Note that all data is of f_y not f_x , and that the y-axis is log-scaled.

This is best indicated by the distributions of surface area size (mm^2) of elicited fMRI activations, following their projection to the cortical surface (means: left hand=322 mm^2 ; right hand=333 mm^2 ; left foot=157 mm^2 ; right foot=220 mm^2 ; tongue=500 mm^2). Shown in Figure 22. Thus, it appears larger motor homunculus areas return a larger fMRI activation. Whilst the mean size of each activated structural module changes similarly between task groups, it is to a lesser extent (means: left hand=69 mm^2 ; right hand=75 mm^2 ; left foot=54 mm^2 ; right foot=69 mm^2 ; tongue=84 mm^2). Secondary to the non-specific nature of functional modules, as described in Figure 21. Multiplying the mean number of structural modules per task by their average size, visually confirms this.

4.2 STRENGTH OF ALIGNMENT OF FUNCTIONAL MODULES TO STRUCTURAL MODULES IS WEAK-MODERATE AND DEPENDENT ON MOTOR-TASK

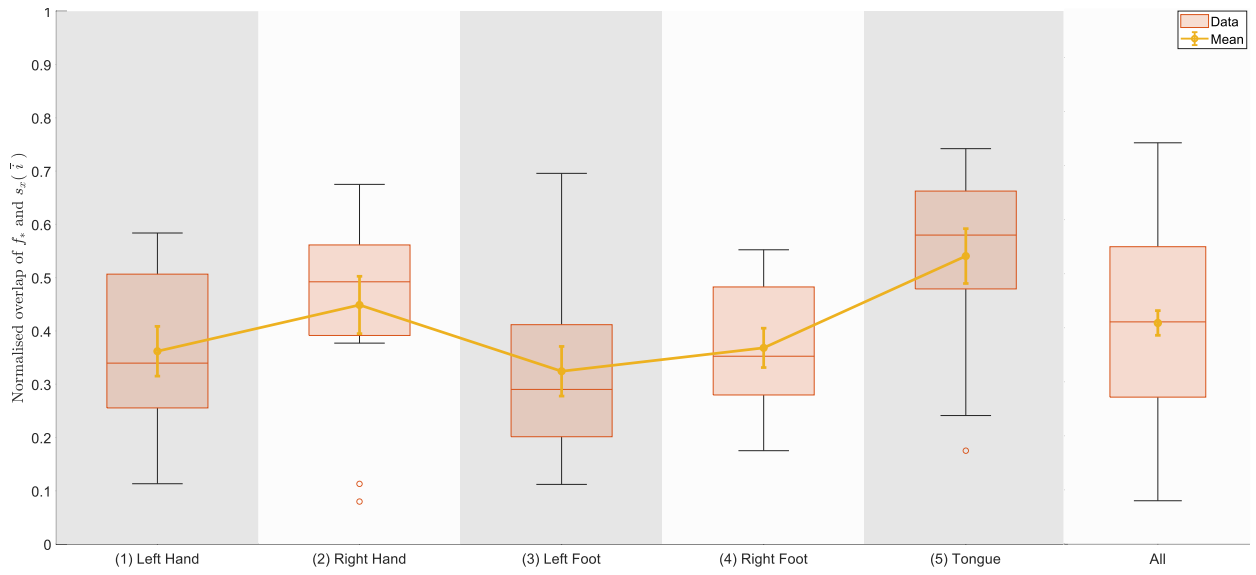


Figure 23: Boxplots showing the normalised, weighted mean of all optimal functional module's (f_*) coverage, \bar{i} , of their underlying structural modules (s_x). Data for all 12 subjects included. The first five columns are distributions of normalised coverages per motor task. The final column shows all data combined. Error bars use standard error of the mean (σ/\sqrt{n}).

A trend for the amount an optimal functional module overlays its corresponding structural modules is not as grossly evident (Figure 23). Nevertheless, it could still be inferred. Whilst tongue-movement elicits the largest normalised functional-structure coverage averaged across all participants (mean=0.5405, SD=0.1782), foot movement yields the smallest coverage (left foot: mean=0.3243, std=0.1614; right foot: mean=0.3682, SD=0.1279). Hand movement sits between (left hand: mean=0.3619, SD=0.1618; right hand: mean=0.4487, SD=0.1864). The coverage is therefore, irrespective of motor task, only moderate-poor (all: mean=0.4087; SD=0.1768).

Table 1: Results of one-sample t-test ($\alpha=0.05$), comparing present \bar{i} against published correlation score of 0.416.

One sample t-test ($\alpha = 0.05$)						
Null hypothesis, $H_0: \bar{i} = \mu_0$ (0.416) Alternative hypothesis, $H_1: \bar{i} > \mu_0$ (0.416).						
Motor task	Mean (\bar{i})	SD (σ)	Sample size (n)	t-score	p-value	Reject H_0 and accept H_1 ?
Left Hand	0.3619	0.1618	12 (df:11)	-1.1583	0.8644	No.
Right Hand	0.4487	0.1864	12 (df:11)	0.6077	0.2779	No.
Left Foot	0.3243	0.1614	12 (df:11)	-1.968	0.9626	No.

Right Foot	0.3682	0.1279	12 (df:11)	-1.2946	0.8890	No.
Tongue	0.5405	0.1782	12 (df:11)	2.42	0.0170	<u>Yes.</u>

We infer that each motor task's normalised overlap (\bar{i}) is a tentative measure of correlation between structure and function. Hence, these values are statistically compared against the correlation co-efficient ($r=0.416$, $p=0$) published by Gu et al. (2021). We first hypothesise that correlation is greater than this, given that Cocchi et al. measured a slightly higher correlation of $r=0.43$ ($p=0.032$) (2014). The results of our one-sample t-test are in Table 1.

Only for tongue-related brain activity can we infer that the correlation between structure and function is greater than $r=0.416$. To accompany this finding, we repeated the calculation for the tongue domain (Table 2). This time, we found evidence to suggest that structure-function coupling is higher than 0.43.

Table 2: Results of one-sample t-test ($\alpha=0.05$), comparing \bar{i} of the tongue against published correlation score of 0.43.

One sample t-test ($\alpha = 0.05$)						
Null hypothesis, $H_0: \bar{i} = \mu_0$ (0.43) Alternative hypothesis, $H_1: \bar{i} > \mu_0$ (0.43).						
Motor task	Mean (\bar{i})	SD (σ)	Sample size (n)	t-score	p-value	Reject H_0 and accept H_1?
Tongue	0.5405	0.1782	12 (df:11)	2.148	0.0274161	<u>Yes.</u>

4.3 COVERAGE OF STRUCTURAL MODULES BY FUNCTIONAL MODULES SHOWS LITTLE INTER-INDIVIDUAL VARIATION

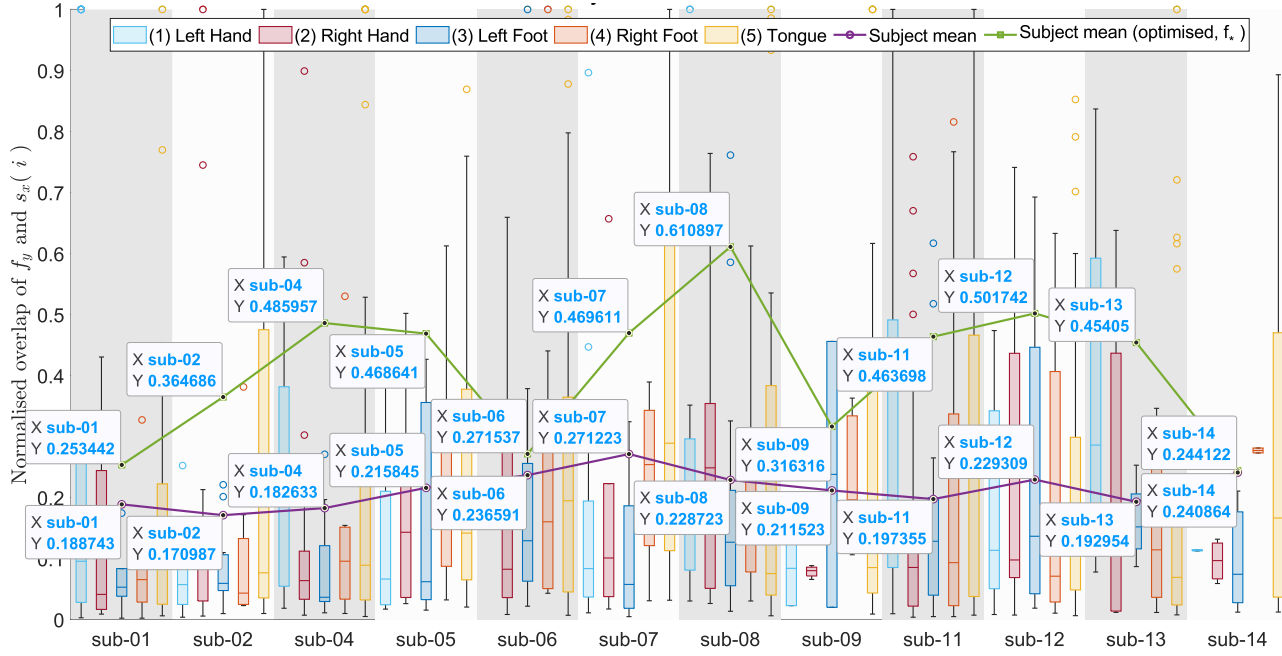


Figure 24: Boxplots for each participant, showing the distribution of their functional modules' (f_y) overlap with underlying structural modules (i), normalised by Equation: 6 and plotted per motor task. Also plotted is a per-subject mean of the structure-function overlap, both for f_y and f_ . Increases in i were found for all subjects following our method of f_* selection.*

The normalised overlap between the two sets of modules was increased for all participants by our selection of f_* (Equation: 6). This is shown in Figure 24 (also plotted per motor task Appendix F).

In the context of all intersections ($s_x \cap f_y$), there was negligible inter-individual variation (mean=0.21390; std=0.02886; co-efficient of variation=0.13492). Upon selection for the optimal functional modules, f_* , slightly higher variance between subject data was observed (mean=0.40870; std=0.11610; co-efficient of variation=0.28407).

5 DISCUSSION

The present work investigated the relationship between structure and function of 12 healthy human brains through novel use of high-resolution connectomics. We developed bespoke coding scripts to superimpose surface-projected fMRI activations onto DWI-derived structural connectomes. Visually, our task-based fMRIs were appropriate localisers of the motor homunculus regions responsible for hands, feet, and tongue movements (e.g., Figure 19 versus Figure 1). We observed non-specificity of fMRI activations for structural modules, and subsequently proposed an approach that optimally selects functional activations so that confounding factors are minimised. Despite sole inclusion of functional modules that overlap best with their structural counterparts, we were unable to completely evidence that structure-function coupling

is greater than that already published, with one exception. Coupling pertinent to tongue movements, perhaps secondary to the size of the related brain areas, has a correlation co-efficient >0.43 (one-sample t-test, $\alpha=0.05$). However, interpretation of the present results should be done cautiously given the reduced statistical power. To the best of our knowledge, this work tackles the scientific inquiry of structure-function relationships of the human brain using new methods that await further refinement, analysis and validation.

5.1 STATISTICAL LIMITATIONS

Despite access to validated brain scans of high quality, this study was limited by its small sample size (participants=12; motor tasks=5). Nevertheless, it serves as a useful preliminary and prompts for the brains of more participants to be processed. It should be noted that, due to the lack of research, we compare the overlap of fMRI activations and structural connectomes (or an interpretation thereof), with the correlation co-efficient of structural-connectivity and functional-connectivity (Gu et al., 2021). Whether network-derived statistics are comparable to spatial metrics in this way remains to be seen.

5.2 LIMITATIONS OF RECONSTRUCTION USING DTI

The production of a structural connectome from DTI data is inherently limited by modern-day tractography. Whilst industry standards defined the optimal parameters of the fibre-tracking algorithm, these values are subject to change with evolving research, as are the models used. It is possible that upon refinement of these, DSI Studio could yield a more (or less) accurate of the structural connectome. Correspondingly, the reconstructed connectomes used in this study would benefit from validation (c.f. Sarwar, Ramamohanarao, et al., 2021).

Our results imply that, in most cases, any given functional module overlaps with numerous structural modules, and only partially (i.e., non-specific and poor-moderate coverage). This could be the reality. Otherwise, and especially pertinent because of this paper's focus on parcellated connectomes, it could be the result of incorrect or poorly defined structural module boundaries. Further experiments and simulations are required using connectomes of different parcellation protocols. Perhaps a connectome parcellated into only 50,000 nodes forces structural modules to be too large. In this way, the present method of assigning streamlines to nearest nodes (to form a binary, undirected network) loses information that is necessary for proper community-detection. An interesting extension of this work would be to mediate the number of parcels of a connectome, and observe for change in the normalised coverage of structural modules by a functional module.

Further still, this study used the Louvain community-detection algorithm, "Louvain Method". Commonly used for its speed and simplicity, we orientate its output towards maximal modularity by leveraging γ . Other algorithms may perform better. Contrary to the argument of experimenting with finer parcellations,

an opposite approach would be to produce fewer, rather than more, modules. Here, changes in the specificity of a functional module could be notable, as a functional module is less likely to overlap with multiple structural modules if there are fewer of them. Clauset et al. propose a heuristic of hierarchical clustering, for example (2008). Theirs is just one example from a family of algorithms that find modularity in different ways, such as functions of node distance and linkage, “agglomerative techniques”, and maximisation of expectation (Motschnig et al., 2021). Most importantly, they can yield modules across many scales simultaneously (Clauset et al., 2008), hence their relevance here.

5.3 LIMITATIONS OF RECONSTRUCTION USING fMRI

Defining modules from fMRI data is also not without its flaws. As previously mentioned, the successful casting of voxels to a surface depends on the dimensions of the initial module (Figure 17), and the independent projection of surface vertexes could be more rigorous. For example, by projecting all modules as one unit to the surface (e.g., using Iso2Mesh’s image registration utility to project vertices, although anatomical landmarks are required). In this way, shapes of functional modules and their distances from each other are proportionally maintained.

Another observation worthy of further experimentation is that the yielded fMRI modules are inherently linked to the parameters (e.g., P_{FWE} , k) used in the GLM model. For instance, as P_{FWE} approaches zero, fMRI modules become smaller and thus our averaged normalised coverage reduces also. Likewise, as P_{FWE} tends towards 1 and the detected fMRI activations grow larger, could the normalised coverage proportionally increase? This could elucidate whether fMRI modules activate binarily, or if there exists a central hotspot of activity within each. This may, however, be tricky to interpret in the context of a rising false positive rate. Alternatively, future researchers may benefit from non-binariised volumes of fMRI activations. Here, they could plot multiple boundaries per functional module, each at a different threshold, and inspect how these boundaries align with structural modules. Documenting the effect of GLM parameters could also reduce noise and aid the selection of f_* , particularly by leveraging k (minimum number of voxels per activation). Using task-specific masks, inspired by the motor homunculus, is another way that irrelevant activations could be filtered.

Perhaps the largest outstanding work for this paper is that of inter-individual comparison. The pipeline inherited from Taylor et al. did not support normalisation of brains to standardised MNI space (2017). Modifying code to enable such support was outside the remit of this work due to time, but should be considered by future researchers. It would enable the averaging of data (anatomical and functional) across participants, as is standard in the literature. This reduces the effect of noise, facilitates appropriate selection of f_* , and reduces the complexity of surface projection. The result would depict the averaged boundaries for structural and functional modules.

6 CONCLUSION

The work presented here is a step forward in understanding how brain function might be constrained by its structure. We have experimented with, and shown the results of, a way to bring together fMRI activations and the connectome into the same anatomical space. Whilst the achieved statistics are underpowered, we hope that our efforts prompt a new wave of research in the area. Publications that propose a validated method of handling multi-modal data for this purpose are non-existent.

Looking ahead, relating structure to function remains as pertinent as ever, especially at high-resolution. Improved scanning power, such as that offered by 7T MRI scanners, may shed new light into the topological organisation of the cortex. Indeed, assisting with the scientific inquiry of the best parcellation protocol that we mentioned earlier. Furthermore, how the relationship between the two levels of abstraction changes with age is also unclear. Some researchers, for example, report that early life adversity can manipulate the structure of the developing brain in such a way that its dysfunction precipitates as mental illness (Kaufman & Charney, 2001). The contribution by altered connectivity to the aetiology of these diseases is yet to be confirmed. Similarly, connectomics may be an efficient and safe tool to measure changes in connectivity for diagnostic utility. For example, aiding the identification, localisation, and/or staging of conductive neuronal tumours (not necessarily limited to the brain).

There is plenty of excitement for connectomes, and the contexts in which they are tested by researchers is bountiful. Despite this, connectomes remain relatively new. The way they are acquired, processed, and interpreted continues to evolve over time with new technology and literary progress. Thus, we conclude by returning to our initial problem: “to what degree does the structural connectome constrain function?” For now, this question’s response is incomplete, answered only partially by this work; however, our results implore further research. It is a large endeavour, to understand “the most complex system in the Animal kingdom” (Batista-García-Ramó & Fernández-Verdecia, 2018), but we hope that this work contributes to the emerging field of connectomics.

REFERENCES

- Abbott, L. F., Bock, D. D., Callaway, E. M., Denk, W., Dulac, C., Fairhall, A. L., Fiete, I., Harris, K. M., Helmstaedter, M., Jain, V., Kasthuri, N., LeCun, Y., Lichtman, J. W., Littlewood, P. B., Luo, L., Maunsell, J. H. R., Reid, R. C., Rosen, B. R., Rubin, G. M., Sejnowski, T. J., Seung, H. S., Svoboda, K., Tank, D. W., Tsao, D., & Van Essen, D. C. (2020, Sep 17). The Mind of a Mouse. *Cell*, 182(6), 1372-1376. <https://doi.org/10.1016/j.cell.2020.08.010>
- Achard, S., & Bullmore, E. (2007, Feb 2). Efficiency and cost of economical brain functional networks. *PLoS Comput Biol*, 3(2), e17. <https://doi.org/10.1371/journal.pcbi.0030017>
- Aguirre, G. K. (2011). Experimental Design and Data Analysis for fMRI. In *Functional Neuroradiology* (pp. 321-330). https://doi.org/10.1007/978-1-4419-0345-7_18
- Baena, V., Schalek, R. L., Lichtman, J. W., & Terasaki, M. (2019). Serial-section electron microscopy using automated tape-collecting ultramicrotome (ATUM). In *Three-Dimensional Electron Microscopy* (pp. 41-67). <https://doi.org/10.1016/bs.mcb.2019.04.004>
- Batista-García-Ramó, K., & Fernández-Verdecia, C. (2018). What We Know About the Brain Structure–Function Relationship. *Behavioral Sciences*, 8(4). <https://doi.org/10.3390/bs8040039>
- Batista-Garcia-Ramo, K., & Fernandez-Verdecia, C. I. (2018, Apr 18). What We Know About the Brain Structure-Function Relationship. *Behav Sci (Basel)*, 8(4). <https://doi.org/10.3390/bs8040039>
- Besson, P., Lopes, R., Leclerc, X., Derambure, P., & Tyvaert, L. (2014, Nov 15). Intra-subject reliability of the high-resolution whole-brain structural connectome. *NeuroImage*, 102 Pt 2, 283-293. <https://doi.org/10.1016/j.neuroimage.2014.07.064>
- Blondel, V. D., Guillaume, J.-L., Lambiotte, R., & Lefebvre, E. (2008). Fast unfolding of communities in large networks. *Journal of Statistical Mechanics: Theory and Experiment*, 2008(10). <https://doi.org/10.1088/1742-5468/2008/10/p10008>
- Bohland, J. W., Wu, C., Barbas, H., Bokil, H., Bota, M., Breiter, H. C., Cline, H. T., Doyle, J. C., Freed, P. J., Greenspan, R. J., Haber, S. N., Hawrylycz, M., Herrera, D. G., Hilgetag, C. C., Huang, Z. J., Jones, A., Jones, E. G., Karten, H. J., Kleinfeld, D., Kotter, R., Lester, H. A., Lin, J. M., Mensh, B. D., Mikula, S., Panksepp, J., Price, J. L., Safdieh, J., Saper, C. B., Schiff, N. D., Schmahmann, J. D., Stillman, B. W., Svoboda, K., Swanson, L. W., Toga, A. W., Van Essen, D. C., Watson, J. D., & Mitra, P. P. (2009, Mar). A proposal for a coordinated effort for the determination of brainwide neuroanatomical connectivity in model organisms at a mesoscopic scale. *PLoS Comput Biol*, 5(3), e1000334. <https://doi.org/10.1371/journal.pcbi.1000334>
- Bullmore, E., & Sporns, O. (2012, Apr 13). The economy of brain network organization. *Nat Rev Neurosci*, 13(5), 336-349. <https://doi.org/10.1038/nrn3214>
- Buzsaki, G., Geisler, C., Henze, D. A., & Wang, X. J. (2004, Apr). Interneuron Diversity series: Circuit complexity and axon wiring economy of cortical interneurons. *Trends Neurosci*, 27(4), 186-193. <https://doi.org/10.1016/j.tins.2004.02.007>

Cherniak, C. (1994, Apr). Component placement optimization in the brain. *J Neurosci*, 14(4), 2418-2427. <https://www.ncbi.nlm.nih.gov/pubmed/8158278>

Churchland, P. S., & Sejnowski, T. J. (1988, Nov 4). Perspectives on cognitive neuroscience. *Science*, 242(4879), 741-745. <https://doi.org/10.1126/science.3055294>

Clarke, E. (1965, Oct). Nicolas Stensen and the Brain [Abstract]. *Proc R Soc Med*, 58(10), 749. <https://www.ncbi.nlm.nih.gov/pubmed/19994453>

Clauset, A., Moore, C., & Newman, M. E. (2008, May 1). Hierarchical structure and the prediction of missing links in networks. *Nature*, 453(7191), 98-101. <https://doi.org/10.1038/nature06830>

Cocchi, L., Harding, I. H., Lord, A., Pantelis, C., Yucel, M., & Zalesky, A. (2014). Disruption of structure-function coupling in the schizophrenia connectome. *Neuroimage Clin*, 4, 779-787. <https://doi.org/10.1016/j.nicl.2014.05.004>

Costanzo, R., Brunasso, L., Paolini, F., Benigno, U. E., Porzio, M., Giammalva, G. R., Gerardi, R. M., Umana, G. E., di Bonaventura, R., Sturiale, C. L., Visocchi, M., Iacopino, D. G., & Maugeri, R. (2022, Aug). Spinal Tractography as a Potential Prognostic Tool in Spinal Cord Injury: A Systematic Review. *World Neurosurg*, 164, 25-32. <https://doi.org/10.1016/j.wneu.2022.04.103>

de Reus, M. A., & van den Heuvel, M. P. (2013, Oct 15). The parcellation-based connectome: limitations and extensions. *NeuroImage*, 80, 397-404. <https://doi.org/10.1016/j.neuroimage.2013.03.053>

Desikan, R. S., Segonne, F., Fischl, B., Quinn, B. T., Dickerson, B. C., Blacker, D., Buckner, R. L., Dale, A. M., Maguire, R. P., Hyman, B. T., Albert, M. S., & Killiany, R. J. (2006, Jul 1). An automated labeling system for subdividing the human cerebral cortex on MRI scans into gyral based regions of interest. *NeuroImage*, 31(3), 968-980. <https://doi.org/10.1016/j.neuroimage.2006.01.021>

Fang-Cheng, Y. (2007). *DSI-Studio: A Tractography Software Tool for Diffusion MRI Analysis*. Retrieved 21/09/2022 from <https://dsi-studio.labsolver.org/>

Fornito, A., Arnatkeviciute, A., & Fulcher, B. D. (2019, Jan). Bridging the Gap between Connectome and Transcriptome. *Trends Cogn Sci*, 23(1), 34-50. <https://doi.org/10.1016/j.tics.2018.10.005>

Friston, K. J., Frith, C. D., Frackowiak, R. S., & Turner, R. (1995, Jun). Characterizing dynamic brain responses with fMRI: a multivariate approach. *NeuroImage*, 2(2), 166-172. <https://doi.org/10.1006/nimg.1995.1019>

Gu, Z., Jamison, K. W., Sabuncu, M. R., & Kuceyeski, A. (2021, Aug 12). Heritability and interindividual variability of regional structure-function coupling. *Nat Commun*, 12(1), 4894. <https://doi.org/10.1038/s41467-021-25184-4>

Harris, K. M., Perry, E., Bourne, J., Feinberg, M., Ostroff, L., & Hurlburt, J. (2006, Nov 22). Uniform serial sectioning for transmission electron microscopy. *J Neurosci*, 26(47), 12101-12103. <https://doi.org/10.1523/JNEUROSCI.3994-06.2006>

Helmstaedter, M., Briggman, K. L., Turaga, S. C., Jain, V., Seung, H. S., & Denk, W. (2013, Aug 8). Connectomic reconstruction of the inner plexiform layer in the mouse retina. *Nature*, 500(7461), 168-174. <https://doi.org/10.1038/nature12346>

Hill, R. (2022). *GitHub - reecehill/Human-Connectome-Investigating-Modularity: My MSc Dissertation: using data from the Human Connectome Project to investigate modularity*. Retrieved 21/09/2022 from <https://github.com/reecehill/Human-Connectome-Investigating-Modularity>

Huisman, T. A. (2010, Oct 4). Diffusion-weighted and diffusion tensor imaging of the brain, made easy. *Cancer Imaging, 10 Spec no A*, S163-171. <https://doi.org/10.1102/1470-7330.2010.9023>

Jahn, A. L., Dan; Holscher, Eric; Johnson, John T.; Sayal, Alexandre; jstaph; JohannesWiesner; Clucas, Jon; Tapera, Tinashe Michael; justbennet;. (2022). *andrewjahn/AndysBrainBook*. Zenodo. Retrieved 25/09/2022 from <https://andysbrainbook.readthedocs.io/>

Jang, S. H., & Seo, Y. S. (2022, May). Diffusion tensor tractography characteristics of axonal injury in concussion/mild traumatic brain injury. *Neural Regen Res*, 17(5), 978-982. <https://doi.org/10.4103/1673-5374.324825>

Josephson, S. A., Papanastassiou, A. M., Berger, M. S., Barbaro, N. M., McDermott, M. W., Hilton, J. F., Miller, B. L., & Geschwind, M. D. (2007, Jan). The diagnostic utility of brain biopsy procedures in patients with rapidly deteriorating neurological conditions or dementia. *J Neurosurg*, 106(1), 72-75. <https://doi.org/10.3171/jns.2007.106.1.72>

Kasthuri, N., & Lichtman, J. W. (2007, Apr). The rise of the 'projectome'. *Nat Methods*, 4(4), 307-308. <https://doi.org/10.1038/nmeth0407-307>

Kaufman, J., & Charney, D. (2001, Summer). Effects of early stress on brain structure and function: implications for understanding the relationship between child maltreatment and depression. *Dev Psychopathol*, 13(3), 451-471. <https://doi.org/10.1017/s0954579401003030>

Kleinfeld, D., Bharioke, A., Blinder, P., Bock, D. D., Briggman, K. L., Chklovskii, D. B., Denk, W., Helmstaedter, M., Kaufhold, J. P., Lee, W. C., Meyer, H. S., Micheva, K. D., Oberlaender, M., Prohaska, S., Reid, R. C., Smith, S. J., Takemura, S., Tsai, P. S., & Sakmann, B. (2011, Nov 9). Large-scale automated histology in the pursuit of connectomes. *J Neurosci*, 31(45), 16125-16138. <https://doi.org/10.1523/JNEUROSCI.4077-11.2011>

Kuwajima, M., Spacek, J., & Harris, K. M. (2013, Oct 22). Beyond counts and shapes: studying pathology of dendritic spines in the context of the surrounding neuropil through serial section electron microscopy. *Neuroscience*, 251, 75-89. <https://doi.org/10.1016/j.neuroscience.2012.04.061>

Latora, V., & Marchiori, M. (2001, Nov 5). Efficient behavior of small-world networks. *Phys Rev Lett*, 87(19), 198701. <https://doi.org/10.1103/PhysRevLett.87.198701>

Liu, T. T. (2016, Dec). Noise contributions to the fMRI signal: An overview. *NeuroImage*, 143, 141-151. <https://doi.org/10.1016/j.neuroimage.2016.09.008>

Magaki, S., Gardner, T., Khanlou, N., Yong, W. H., Salamon, N., & Vinters, H. V. (2015, Apr). Brain biopsy in neurologic decline of unknown etiology. *Hum Pathol*, 46(4), 499-506. <https://doi.org/10.1016/j.humpath.2014.12.003>

Maynert, T. (2018). *Psychiatry, a Clinical Treatise on Disease of the Fore-Brain, based upon a Study of its Structure, Functions, and Nutrition. By Theodore Meynert, M.D. Translated by B. Sachs, M.D. Part I.—The Anatomy, Physiology, and Chemistry of the Brain* (Vol. 32). <https://doi.org/10.1192/bjp.32.139.400>

Meoded, A., Huisman, T., Casamassima, M. G. S., Jallo, G. I., & Poretti, A. (2017, May). The structural connectome in children: basic concepts, how to build it, and synopsis of challenges for the developing pediatric brain. *Neuroradiology*, 59(5), 445-460. <https://doi.org/10.1007/s00234-017-1831-1>

Meunier, D., Lambiotte, R., Fornito, A., Ersche, K. D., & Bullmore, E. T. (2009). Hierarchical modularity in human brain functional networks. *Front Neuroinform*, 3, 37. <https://doi.org/10.3389/neuro.11.037.2009>

Mikula, S., Binding, J., & Denk, W. (2012, Dec). Staining and embedding the whole mouse brain for electron microscopy. *Nat Methods*, 9(12), 1198-1201. <https://doi.org/10.1038/nmeth.2213>

Mori, S., & Zhang, J. (2006, Sep 7). Principles of diffusion tensor imaging and its applications to basic neuroscience research. *Neuron*, 51(5), 527-539. <https://doi.org/10.1016/j.neuron.2006.08.012>

Motschnig, N., Ramharter, A., Schweiger, O., Zabka, P., & Foerster, K.-T. (2021). *On Comparing and Enhancing Two Common Approaches to Network Community Detection* 2021 IEEE Global Communications Conference (GLOBECOM),

Nicholas, J., Johannessen, A. M., Nunen, T. V. (2019). *Tactile Working Memory Scale: A Professional Manual*. Nordens välfärdscenter / Nordic Welfare Centre.

NIH Blueprint. (2010). *Connectome Programs | Blueprint*. Retrieved 31/08/2022 from <https://neuroscienceblueprint.nih.gov/human-connectome/connectome-programs>

Nitta, Y., & Sugie, A. (2022, Dec). Studies of neurodegenerative diseases using *Drosophila* and the development of novel approaches for their analysis. *Fly (Austin)*, 16(1), 275-298. <https://doi.org/10.1080/19336934.2022.2087484>

Ohno, N., Katoh, M., Saitoh, Y., Saitoh, S., & Ohno, S. (2015, Feb). Three-dimensional volume imaging with electron microscopy toward connectome. *Microscopy (Oxf)*, 64(1), 17-26. <https://doi.org/10.1093/jmicro/dfu112>

Oldfield, R. C. (1971, Mar). The assessment and analysis of handedness: the Edinburgh inventory. *Neuropsychologia*, 9(1), 97-113. [https://doi.org/10.1016/0028-3932\(71\)90067-4](https://doi.org/10.1016/0028-3932(71)90067-4)

Pajevic, S., & Pierpaoli, C. (1999, Sep). Color schemes to represent the orientation of anisotropic tissues from diffusion tensor data: application to white matter fiber tract mapping in the human brain. *Magn Reson Med*, 42(3), 526-540. <https://www.ncbi.nlm.nih.gov/pubmed/10467297>

Parent, A. (2013, Jul). Niels Stensen: a 17th century scientist with a modern view of brain organization. *Can J Neurol Sci*, 40(4), 482-492. <https://doi.org/10.1017/s0317167100014566>

Pinho, A. L., Amadon, A., Fabre, M., Dohmatob, E., Denghien, I., Torre, J. J., Ginisty, C., Becuwe-Desmidt, S., Roger, S., Laurier, L., Joly-Testault, V., Mediouni-Cloarec, G., Double, C., Martins, B., Pinel, P., Eger, E., Varoquaux, G., Pallier, C., Dehaene, S., Hertz-Pannier, L., & Thirion, B. (2021, Mar). Subject-specific segregation of functional territories based on deep phenotyping. *Hum Brain Mapp*, 42(4), 841-870. <https://doi.org/10.1002/hbm.25189>

Pinho, A. L., Amadon, A., Ruest, T., Fabre, M., Dohmatob, E., Denghien, I., Ginisty, C., Becuwe-Desmidt, S., Roger, S., Laurier, L., Joly-Testault, V., Mediouni-Cloarec, G., Double, C., Martins, B., Pinel, P., Eger, E., Varoquaux, G., Pallier, C., Dehaene, S., Hertz-Pannier, L., & Thirion, B. (2018, Jun 12). Individual Brain Charting, a high-resolution fMRI dataset for cognitive mapping. *Sci Data*, 5(1), 180105. <https://doi.org/10.1038/sdata.2018.105>

Pinho, A. L., Torre, J. J., Shankar, S., & Thirion, B. (2020). *Dataset Documentation, version 3.2* https://project.inria.fr/IBC/files/2020/10/documentation_vs_3-2.pdf

Qianqian, F., & Boas, D. A. (2009). *Tetrahedral mesh generation from volumetric binary and grayscale images* 2009 IEEE International Symposium on Biomedical Imaging: From Nano to Macro,

Rubinov, M., & Sporns, O. (2010, Sep). Complex network measures of brain connectivity: uses and interpretations. *NeuroImage*, 52(3), 1059-1069. <https://doi.org/10.1016/j.neuroimage.2009.10.003>

Sarwar, T., Ramamohanarao, K., & Zalesky, A. (2021, Dec). A critical review of connectome validation studies. *NMR Biomed*, 34(12), e4605. <https://doi.org/10.1002/nbm.4605>

Sarwar, T., Tian, Y., Yeo, B. T. T., Ramamohanarao, K., & Zalesky, A. (2021, Feb 1). Structure-function coupling in the human connectome: A machine learning approach. *NeuroImage*, 226, 117609. <https://doi.org/10.1016/j.neuroimage.2020.117609>

Scheffer, L. K., & Meinertzhagen, I. A. (2021, Nov 1). A connectome is not enough - what is still needed to understand the brain of *Drosophila*? *J Exp Biol*, 224(21). <https://doi.org/10.1242/jeb.242740>

Scheffer, L. K., Xu, C. S., Januszewski, M., Lu, Z., Takemura, S.-y., Hayworth, K. J., Huang, G. B., Shinomiya, K., Maitin-Shepard, J., Berg, S., Clements, J., Hubbard, P., Katz, W., Umayam, L., Zhao, T., Ackerman, D., Blakely, T., Bogovic, J., Dolafi, T., Kainmueller, D., Kawase, T., Khairy, K. A., Leavitt, L., Li, P. H., Lindsey, L., Neubarth, N., Olbris, D. J., Otsuna, H., Trautman, E. T., Ito, M., Goldammer, J., Wolff, T., Svirskas, R., Schlegel, P., Neace, E. R., Knecht, C. J., Alvarado, C. X., Bailey, D. A., Ballinger, S., Borycz, J. A., Canino, B. S., Cheatham, N., Cook, M., Dreher, M., Duclos, O., Eubanks, B., Fairbanks, K., Finley, S., Forknall, N., Francis, A., Hopkins, G. P., Joyce, E. M., Kim, S., Kirk, N. A., Kovalyak, J., Lauchie, S. A., Lohff, A., Maldonado, C., Manley, E. A., McLin, S., Mooney, C., Ndama, M., Ogundeyi, O., Okeoma, N., Ordish, C., Padilla, N., Patrick, C., Paterson, T., Phillips, E. E., Phillips, E. M., Rampally, N., Ribeiro, C., Robertson, M. K., Rymer, J. T., Ryan, S. M., Sammons, M., Scott, A. K., Scott, A. L., Shinomiya, A., Smith, C., Smith, K.,

Smith, N. L., Sobeski, M. A., Suleiman, A., Swift, J., Takemura, S., Talebi, I., Tarnogorska, D., Tenshaw, E., Tokhi, T., Walsh, J. J., Yang, T., Horne, J. A., Li, F., Parekh, R., Rivlin, P. K., Jayaraman, V., Ito, K., Saalfeld, S., George, R., Meinertzhagen, I. A., Rubin, G. M., Hess, H. F., Jain, V., & Plaza, S. M. (2020). <https://doi.org/10.1101/2020.04.07.030213>

Schuette, A. J., Taub, J. S., Hadjipanayis, C. G., & Olson, J. J. (2010, Aug 3). Open biopsy in patients with acute progressive neurologic decline and absence of mass lesion. *Neurology*, 75(5), 419-424. <https://doi.org/10.1212/WNL.0b013e3181eb5889>

Sejnowski, T. J. (2016). Nanoconnectomics. In H. Kennedy, D. C. Van Essen, & Y. Christen (Eds.), *Micro-, Meso- and Macro-Connectomics of the Brain* (pp. 1-10). https://doi.org/10.1007/978-3-319-27777-6_1

Shahhosseini, Y., & Miranda, M. F. (2022, Mar 11). Functional Connectivity Methods and Their Applications in fMRI Data. *Entropy (Basel)*, 24(3). <https://doi.org/10.3390/e24030390>

Sladky, R., Friston, K. J., Trostl, J., Cunnington, R., Moser, E., & Windischberger, C. (2011, Sep 15). Slice-timing effects and their correction in functional MRI. *NeuroImage*, 58(2), 588-594. <https://doi.org/10.1016/j.neuroimage.2011.06.078>

Sporns, O. (2016). Connectome Networks: From Cells to Systems. In H. Kennedy, D. C. Van Essen, & Y. Christen (Eds.), *Micro-, Meso- and Macro-Connectomics of the Brain* (pp. 107-127). https://doi.org/10.1007/978-3-319-27777-6_8

Sporns, O., Tononi, G., & Kotter, R. (2005, Sep). The human connectome: A structural description of the human brain. *PLoS Comput Biol*, 1(4), e42. <https://doi.org/10.1371/journal.pcbi.0010042>

Sporns, O., & Van Den Heuvel, M. P. (2013). Network maps of the human brain's rich club. *Network Science*, 1(2), 248-250. <https://doi.org/10.1017/nws.2013.8>

Sporns, O., & Zwi, J. D. (2004). The small world of the cerebral cortex. *Neuroinformatics*, 2(2), 145-162. <https://doi.org/10.1385/NI:2:2:145>

Steensen, N., & Andrault, R. (2009). *Discours sur l'anatomie du cerveau [1669] présenté et annoté par Raphaële Andrault*. Éd. Classiques Garnier.

Takemura, S. Y., Bharioke, A., Lu, Z., Nern, A., Vitaladevuni, S., Rivlin, P. K., Katz, W. T., Olbris, D. J., Plaza, S. M., Winston, P., Zhao, T., Horne, J. A., Fetter, R. D., Takemura, S., Blazek, K., Chang, L. A., Ogundeyi, O., Saunders, M. A., Shapiro, V., Sigmund, C., Rubin, G. M., Scheffer, L. K., Meinertzhagen, I. A., & Chklovskii, D. B. (2013, Aug 8). A visual motion detection circuit suggested by Drosophila connectomics. *Nature*, 500(7461), 175-181. <https://doi.org/10.1038/nature12450>

Taylor, P. N., Wang, Y., & Kaiser, M. (2017, Jan 5). Within brain area tractography suggests local modularity using high resolution connectomics. *Sci Rep*, 7(1), 39859. <https://doi.org/10.1038/srep39859>

Toescu, S. M., Hales, P. W., Tisdall, M. M., Aquilina, K., & Clark, C. A. (2021, Aug). Neurosurgical applications of tractography in the UK. *Br J Neurosurg*, 35(4), 424-429. <https://doi.org/10.1080/02688697.2020.1849542>

Van Essen, D. C., Glasser, M. F., Dierker, D. L., Harwell, J., & Coalson, T. (2012, Oct). Parcellations and hemispheric asymmetries of human cerebral cortex analyzed on surface-based atlases. *Cereb Cortex*, 22(10), 2241-2262. <https://doi.org/10.1093/cercor/bhr291>

Van Essen, D. C., & Ugurbil, K. (2012, Aug 15). The future of the human connectome. *NeuroImage*, 62(2), 1299-1310. <https://doi.org/10.1016/j.neuroimage.2012.01.032>

Van Essen, D. C., Ugurbil, K., Auerbach, E., Barch, D., Behrens, T. E., Bucholz, R., Chang, A., Chen, L., Corbetta, M., Curtiss, S. W., Della Penna, S., Feinberg, D., Glasser, M. F., Harel, N., Heath, A. C., Larson-Prior, L., Marcus, D., Michalareas, G., Moeller, S., Oostenveld, R., Petersen, S. E., Prior, F., Schlaggar, B. L., Smith, S. M., Snyder, A. Z., Xu, J., Yacoub, E., & Consortium, W. U.-M. H. (2012, Oct 1). The Human Connectome Project: a data acquisition perspective. *NeuroImage*, 62(4), 2222-2231. <https://doi.org/10.1016/j.neuroimage.2012.02.018>

Watts, D. J., & Strogatz, S. H. (1998, Jun 4). Collective dynamics of 'small-world' networks. *Nature*, 393(6684), 440-442. <https://doi.org/10.1038/30918>

White, J. G., Southgate, E., Thomson, J. N., & Brenner, S. (1986, Nov 12). The structure of the nervous system of the nematode *Caenorhabditis elegans*. *Philos Trans R Soc Lond B Biol Sci*, 314(1165), 1-340. <https://doi.org/10.1098/rstb.1986.0056>

Yamada, K., Sakai, K., Akazawa, K., Yuen, S., & Nishimura, T. (2009). MR tractography: a review of its clinical applications. *Magn Reson Med Sci*, 8(4), 165-174. <https://doi.org/10.2463/mrms.8.165>

Yeh, F. C., Wedeen, V. J., & Tseng, W. Y. (2010, Sep). Generalized q-sampling imaging. *IEEE Trans Med Imaging*, 29(9), 1626-1635. <https://doi.org/10.1109/TMI.2010.2045126>

Zhao, L., Guan, M., Zhu, X., Karama, S., Khundrakpam, B., Wang, M., Dong, M., Qin, W., Tian, J., Evans, A. C., & Shi, D. (2015). Aberrant Topological Patterns of Structural Cortical Networks in Psychogenic Erectile Dysfunction. *Front Hum Neurosci*, 9, 675. <https://doi.org/10.3389/fnhum.2015.00675>

Zheng, Z., Lauritzen, J. S., Perlman, E., Robinson, C. G., Nichols, M., Milkie, D., Torrens, O., Price, J., Fisher, C. B., Sharifi, N., Calle-Schuler, S. A., Kmecova, L., Ali, I. J., Karsh, B., Trautman, E. T., Bogovic, J. A., Hanslovsky, P., Jefferis, G., Kazhdan, M., Khairy, K., Saalfeld, S., Fetter, R. D., & Bock, D. D. (2018, Jul 26). A Complete Electron Microscopy Volume of the Brain of Adult *Drosophila melanogaster*. *Cell*, 174(3), 730-743 e722. <https://doi.org/10.1016/j.cell.2018.06.019>

7 APPENDIX A

7.1 SEARCH QUERIES FOR LITERATURE REVIEWS

7.1.1 Nanoconnectomes

We performed a brief literature search using Google Scholar's (<https://scholar.google.com>) advanced search. We searched for any type of article for content (title, abstract and in-text) that matched the following query: "*nanoconnectomic*" OR "*nanoconnectome*" OR "*nano-connectome*" OR "*nano-connectome*" OR "*nano connectome*" OR ("*nano*" AND "*connectome*"). We found 194 results.

7.1.2 Connectomes

We performed a brief literature search using Google Scholar's (<https://scholar.google.com>) advanced search. We searched for any type of article for content (title, abstract and in-text) that matched the following query: "*connectome*". We found 37,600 results.

8 APPENDIX B

8.1 PARTICIPANT INFORMATION

Table 3: Participant demographics. Reproduced from (Pinho et al., 2020).

<u>Subject ID</u>	<u>Year of recruitment</u>	<u>Age at recruitment (years)</u>	<u>Sex</u>	<u>Handedness score</u>
Sub-01	2015	39.5	M	0.3
Sub-02	2015	32.8	M	1
Sub-03	Data unavailable (participant not included in this study).			
Sub-04	2015	26.9	M	0.8
Sub-05	2015	27.4	M	0.6
Sub-06	2015	33.1	M	0.7
Sub-07	2015	38.8	M	1
Sub-08	2015	36.5	F	1
Sub-09	2015	38.5	F	1
Sub-10	Data unavailable (participant not included in this study).			
Sub-11	2016	35.8	M	1
Sub-12	2016	40.8	M	1
Sub-13	2016	28.2	M	0.6
Sub-14	2016	28.3	M	0.7

9 APPENDIX C

9.1 MRI SCANNING PROTOCOLS

9.1.1 High-resolution diffusion data

<u>Parameter</u>	<u>Value</u>
TR	7000ms
TE	76ms
Flip angle	90 deg
Refocusing flip angle	180 deg
FOV	240x240mm
Matrix	128x128
Slice thickness	1.30mm, 112 slices, 1.30mm isotropic
Multiband accel. Factor	2
Echo spacing	0.71ms
BW	1598Hz/Px
Phase partial Fourier	6/8
b-values	[1500, 3000] s/mm ²

9.1.2 High-resolution T1 data

<u>Parameter</u>	<u>Value</u>
TR	2300ms
TE	3.16ms
Flip angle	9 deg
FOV	240x240mm
Matrix	128x128
Slice thickness	0.75mm, 224 slices, 0.75mm isotropic
Multiband accel. Factor	1
Echo spacing	7.8ms
BW	240Hz/Px
Phase partial Fourier	7/8
b-values	0 s/mm ²

9.1.3 T2 SPC data

<u>Parameter</u>	<u>Value</u>
TR	3200ms
TE	419ms
Flip angle mode	T2 var
Refocusing flip angle	180 deg
FOV	230x230mm
Matrix	256x256
Slice thickness	0.9mm, 176 slices, 0.90mm isotropic
Multiband accel. Factor	1
Echo spacing	3.52ms
BW	698Hz/Px
Phase partial Fourier	None
b-values	0 s/mm ²

9.1.4 fMRI data for all motor tasks

<u>Parameter</u>	<u>Value</u>
TR	185ms
TE	27ms
Flip angle mode	74 def
FOV	192x192mm
Matrix	128x128
Slice thickness	1.50mm, 93 slices, 1.50mm isotropic
Multiband accel. Factor	3
Echo spacing	0.65ms
BW	1776Hz/Px
Phase partial Fourier	None
b-values	0 s/mm ²

10 APPENDIX D

10.1 CONNECTIVITY MATRICES

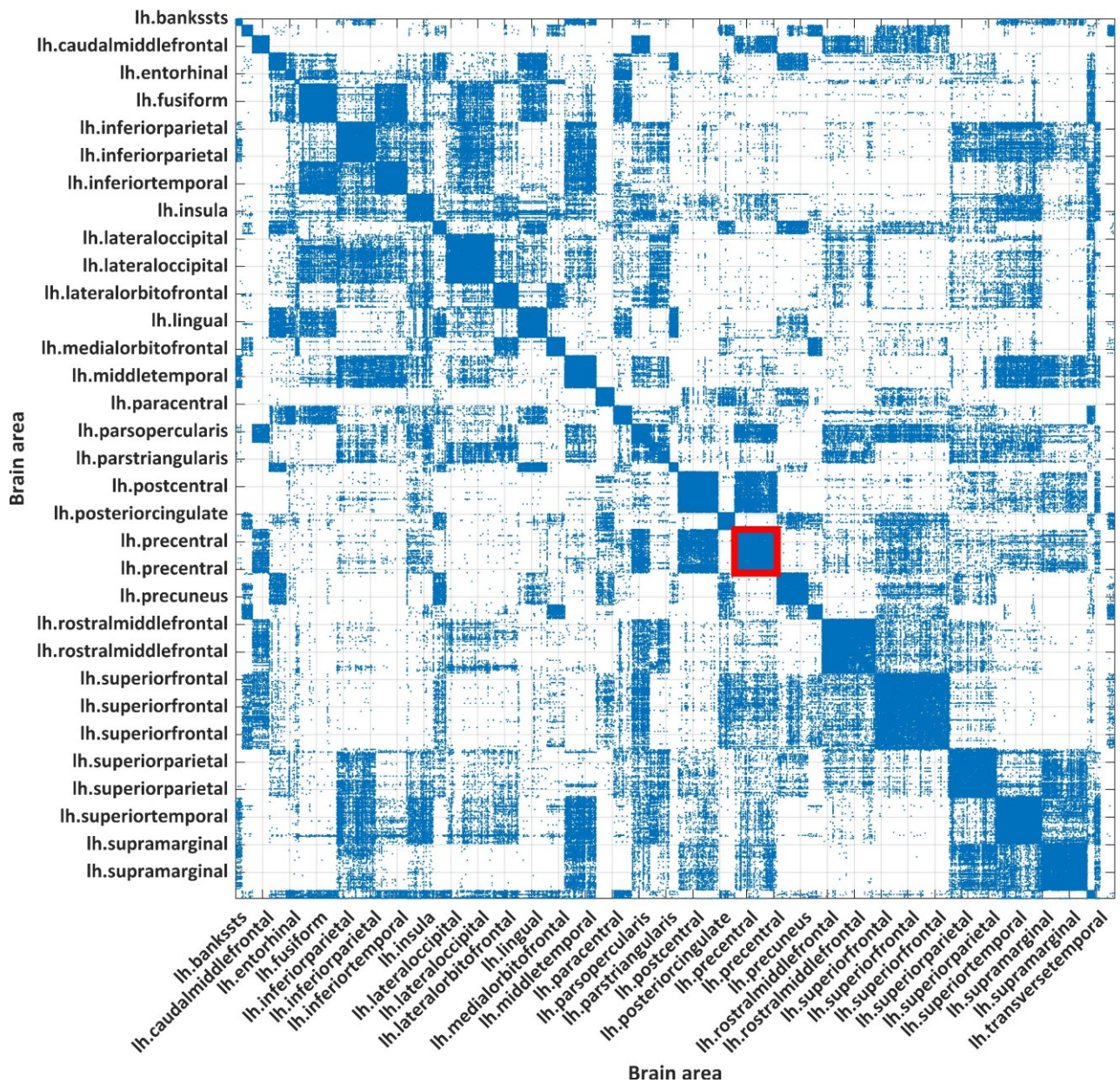


Figure 25: High-resolution connectivity matrix of one subject's (ID: 01) left cortex.

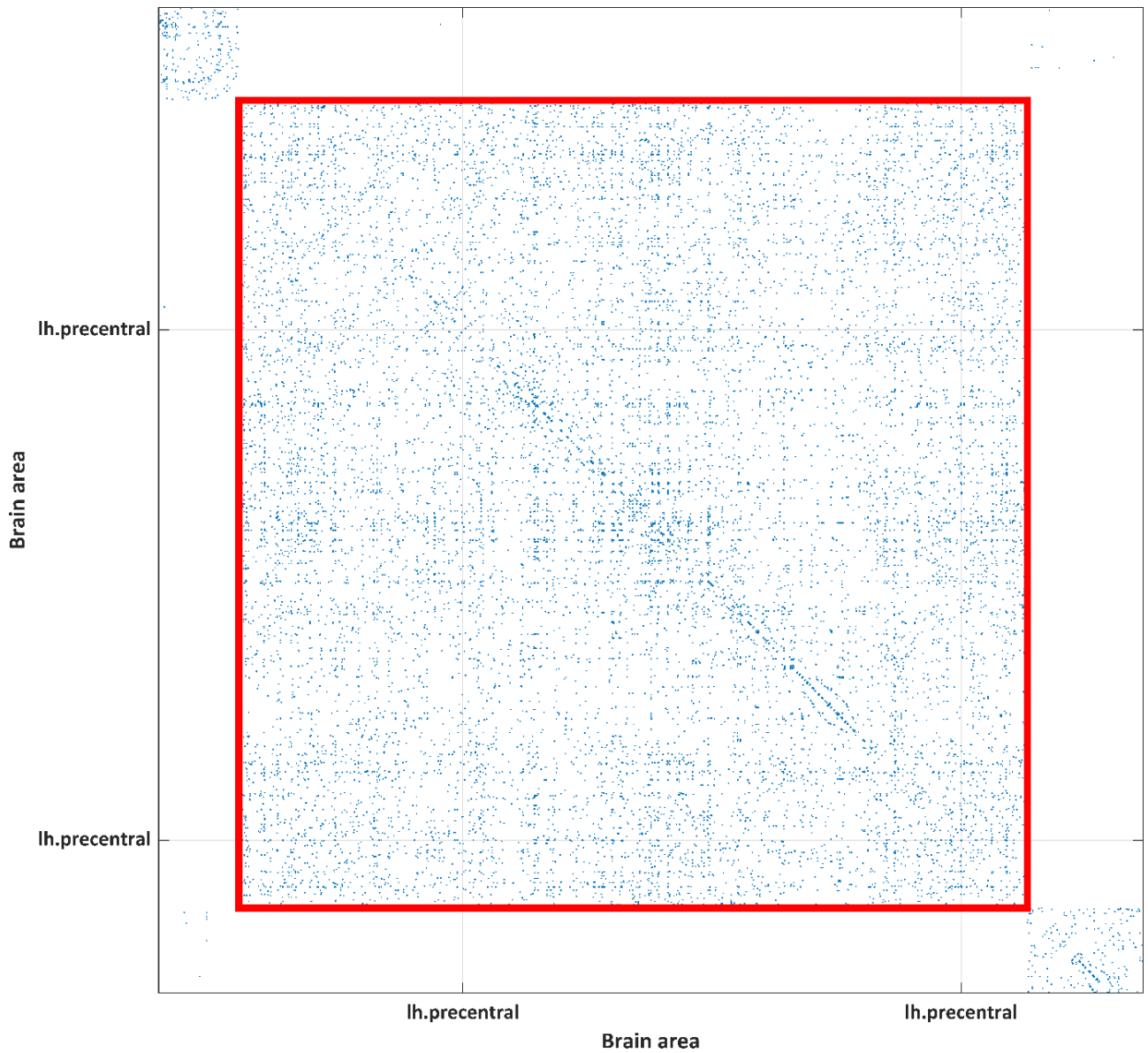
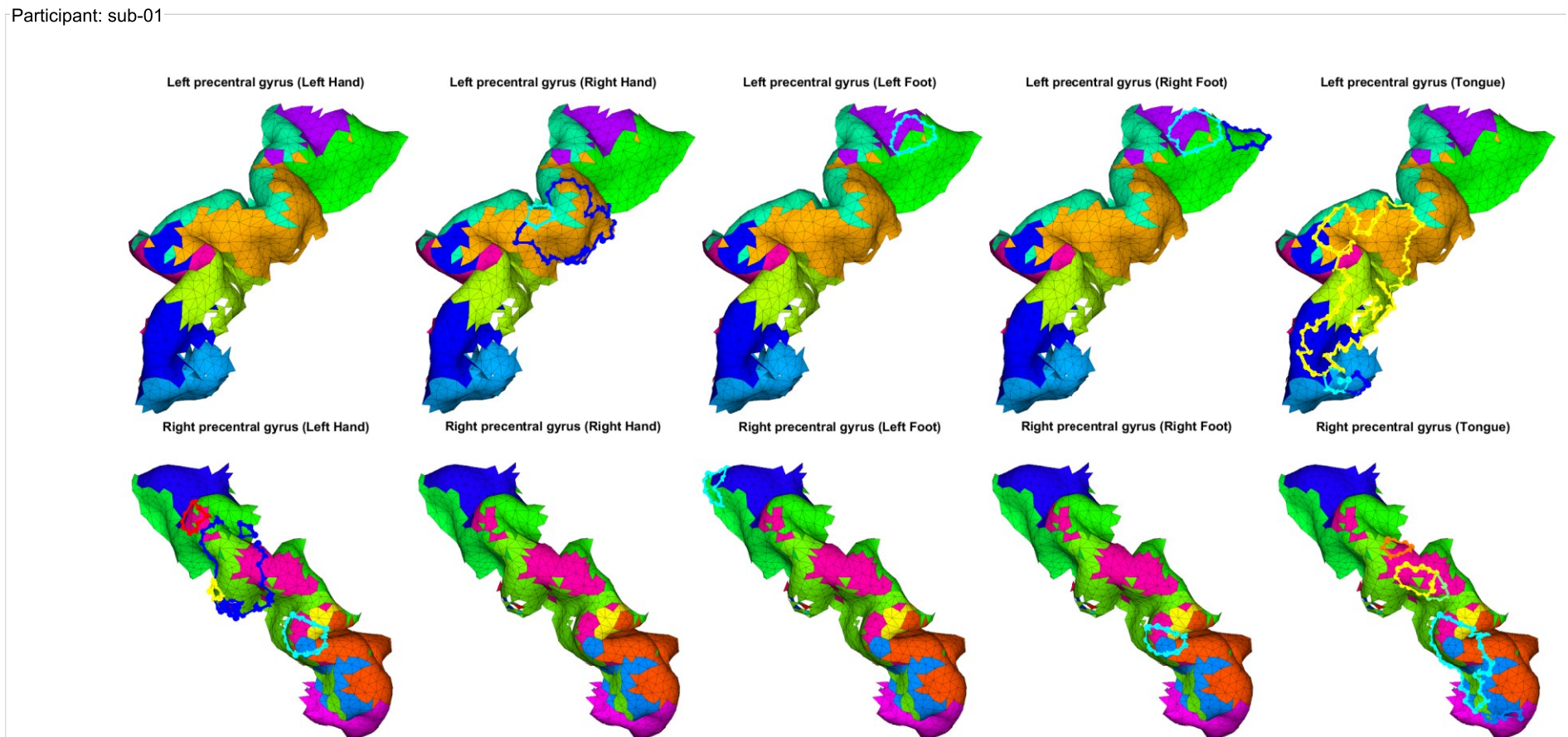


Figure 26: Local (precentral gyrus) connectivity matrix of one subject's (ID: 01) left hemisphere.

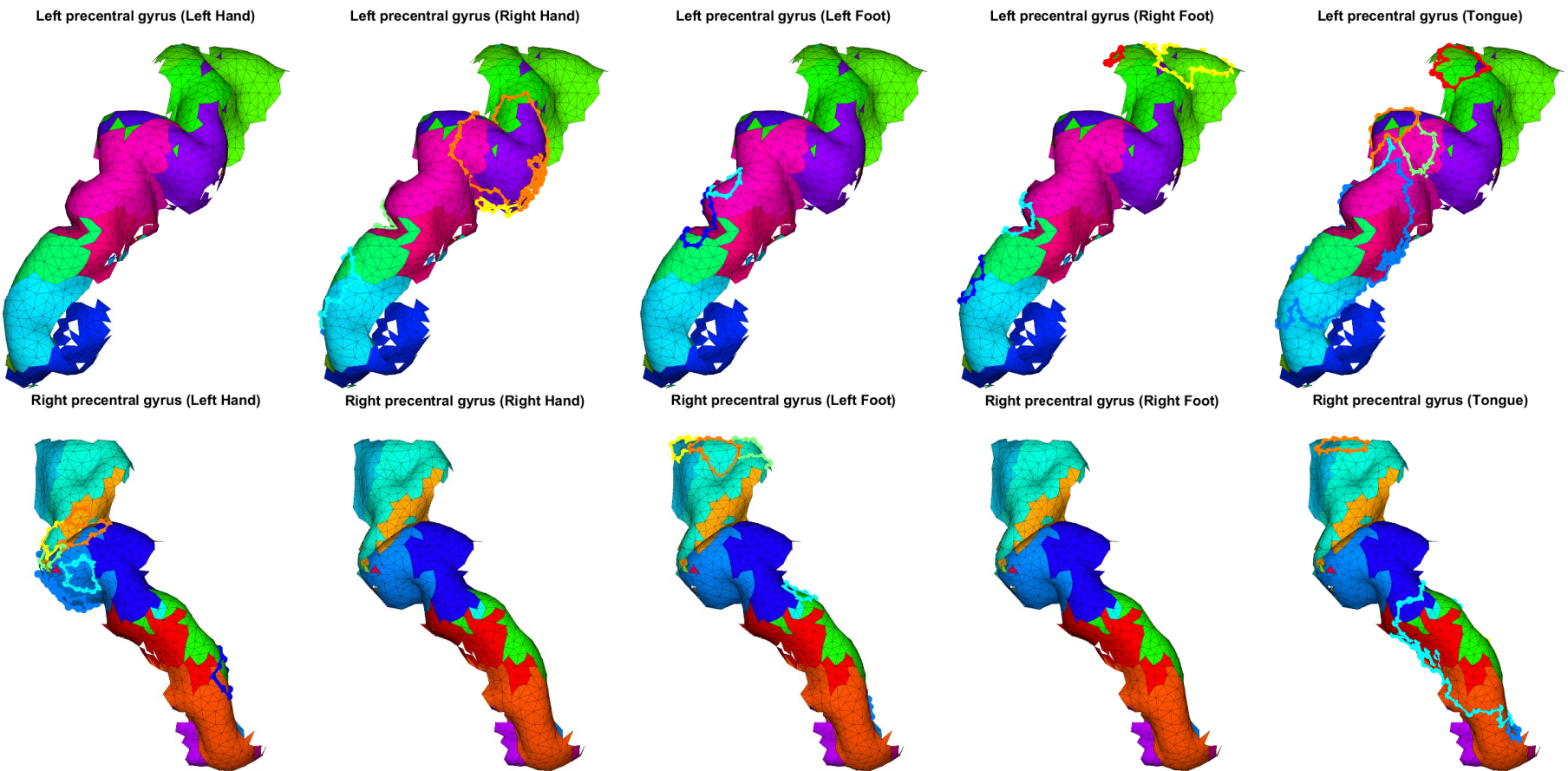
11 APPENDIX E

11.1 STRUCTURAL AND FUNCTIONAL MODULES PER PARTICIPANT

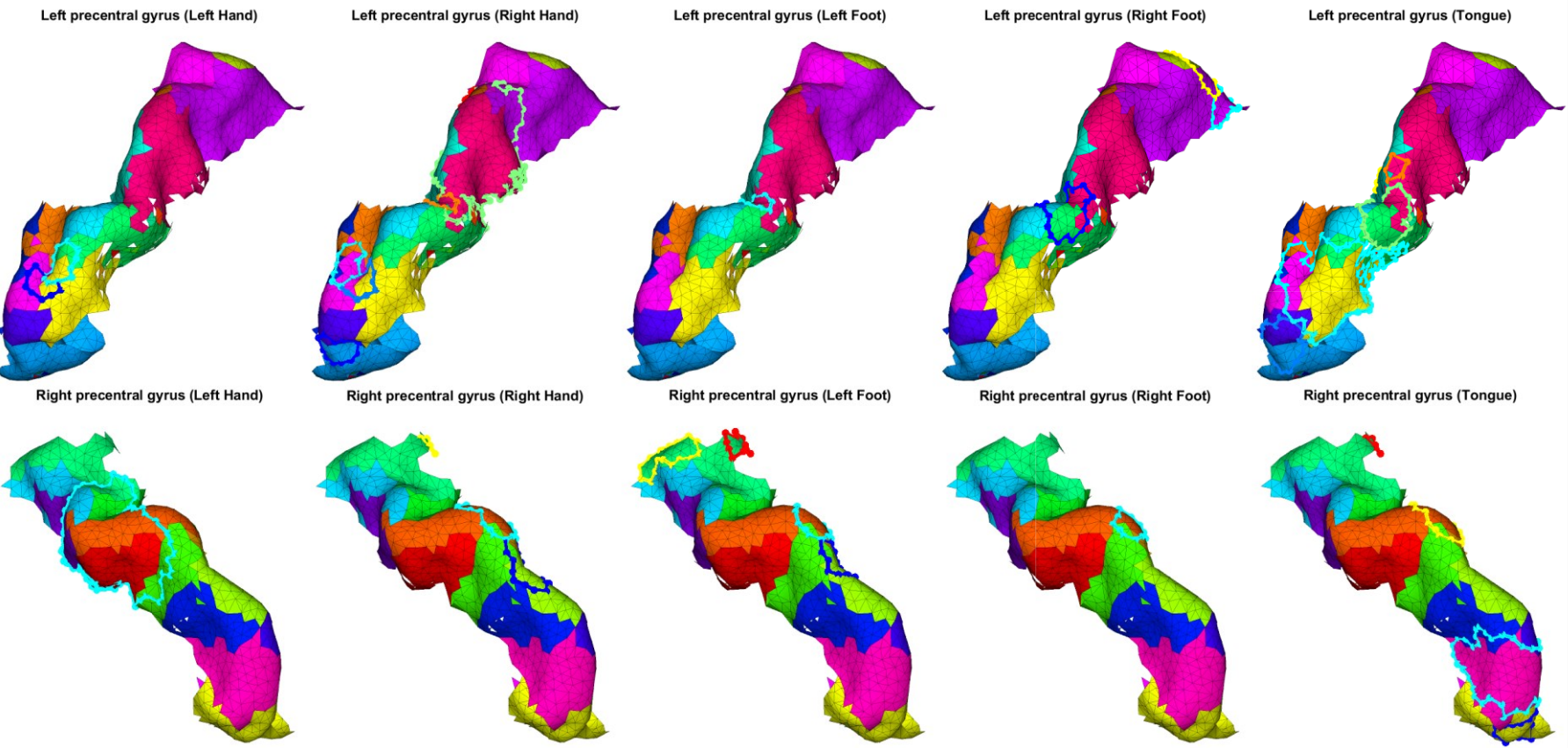
All twelve subjects have their structural and functional modules displayed below. All are suitable substitutes for the “magnified view” of Figure 11, and thus meanings of colours etc. are identical. Note that participants will have different modules, therefore colours between subjects are inconsistent.



Participant: sub-02

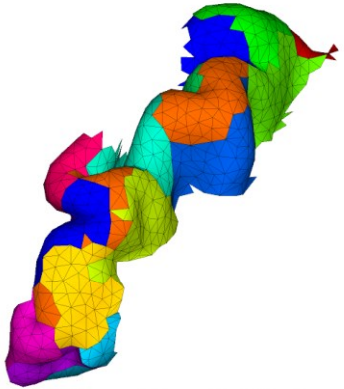


Participant: sub-04

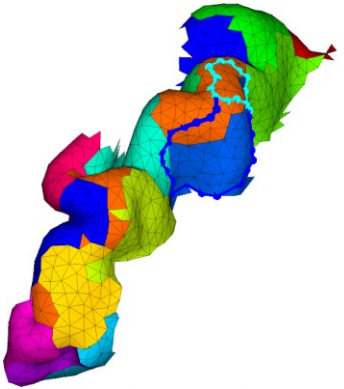


Participant: sub-05

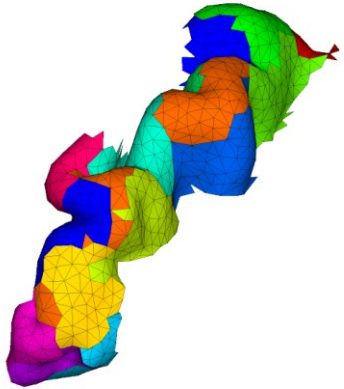
Left precentral gyrus (Left Hand)



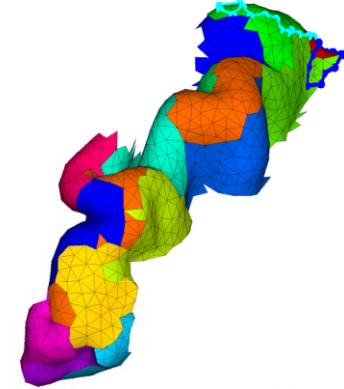
Left precentral gyrus (Right Hand)



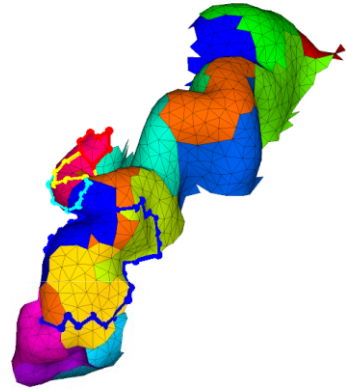
Left precentral gyrus (Left Foot)



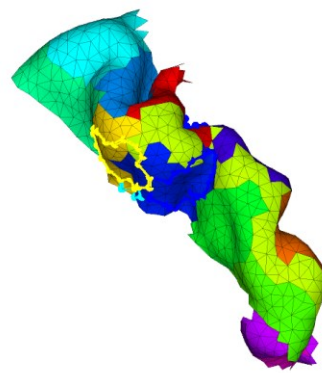
Left precentral gyrus (Right Foot)



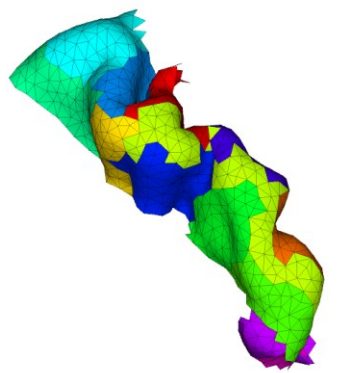
Left precentral gyrus (Tongue)



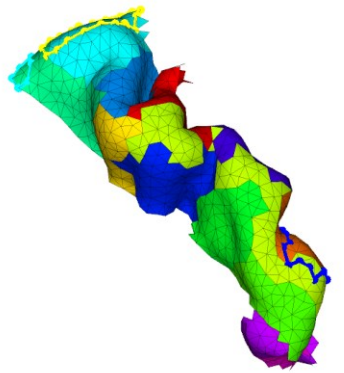
Right precentral gyrus (Left Hand)



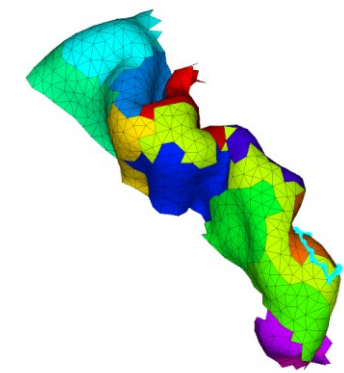
Right precentral gyrus (Right Hand)



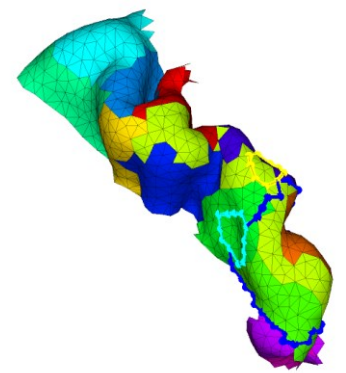
Right precentral gyrus (Left Foot)



Right precentral gyrus (Right Foot)

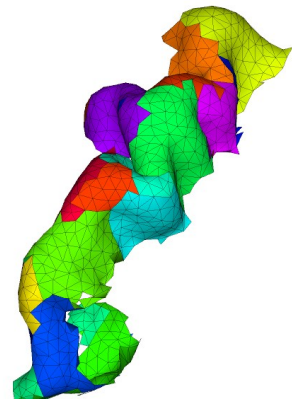


Right precentral gyrus (Tongue)

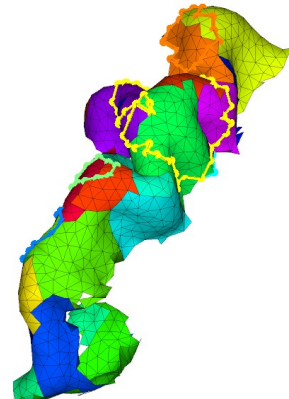


Participant: sub-06

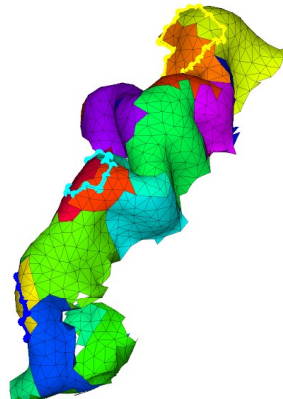
Left precentral gyrus (Left Hand)



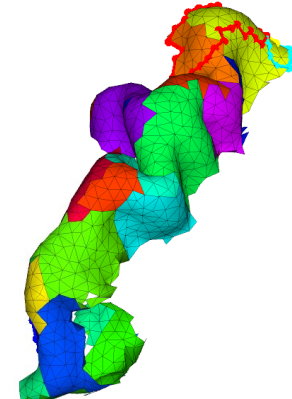
Left precentral gyrus (Right Hand)



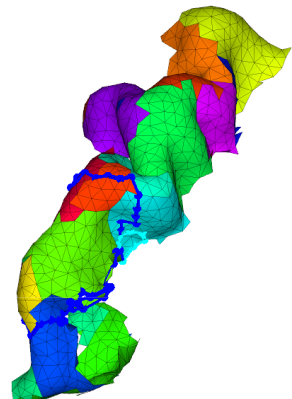
Left precentral gyrus (Left Foot)



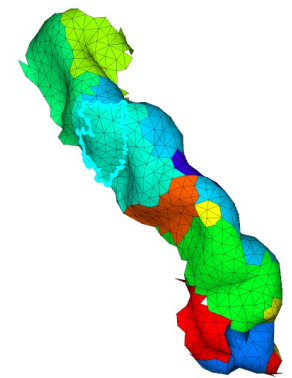
Left precentral gyrus (Right Foot)



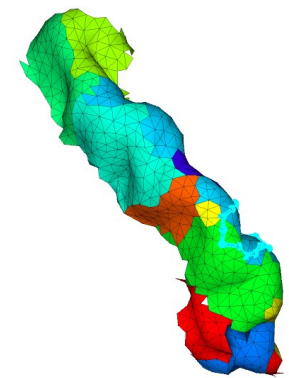
Left precentral gyrus (Tongue)



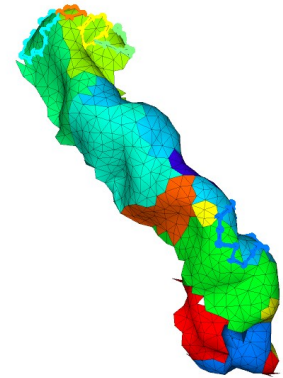
Right precentral gyrus (Left Hand)



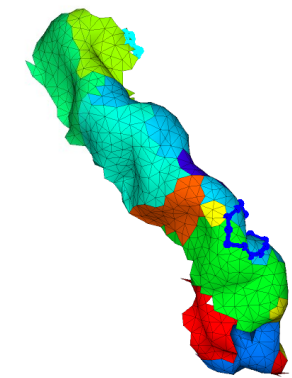
Right precentral gyrus (Right Hand)



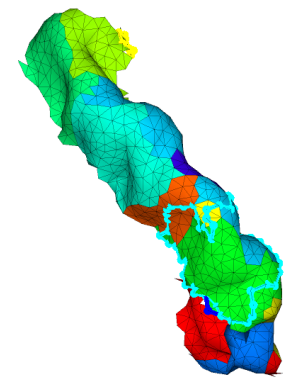
Right precentral gyrus (Left Foot)



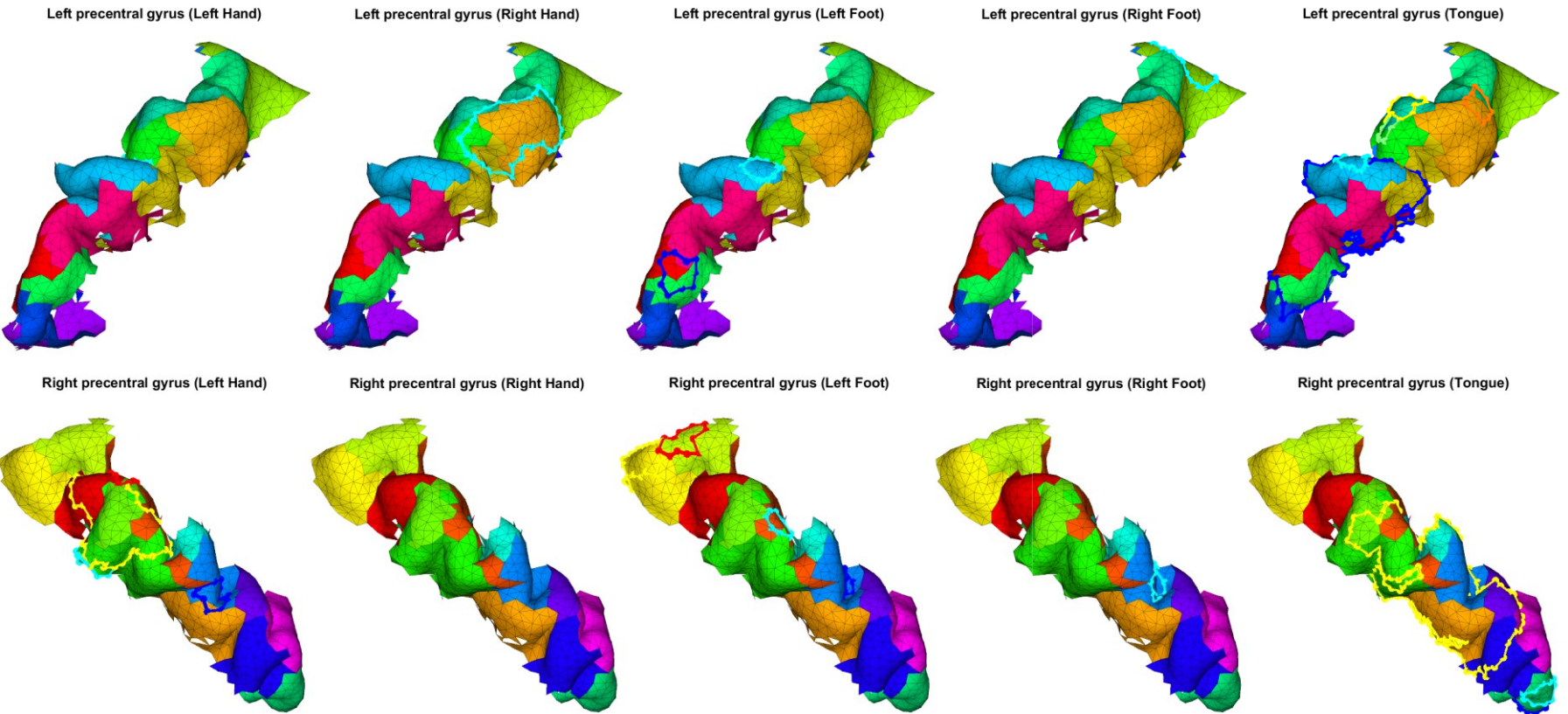
Right precentral gyrus (Right Foot)



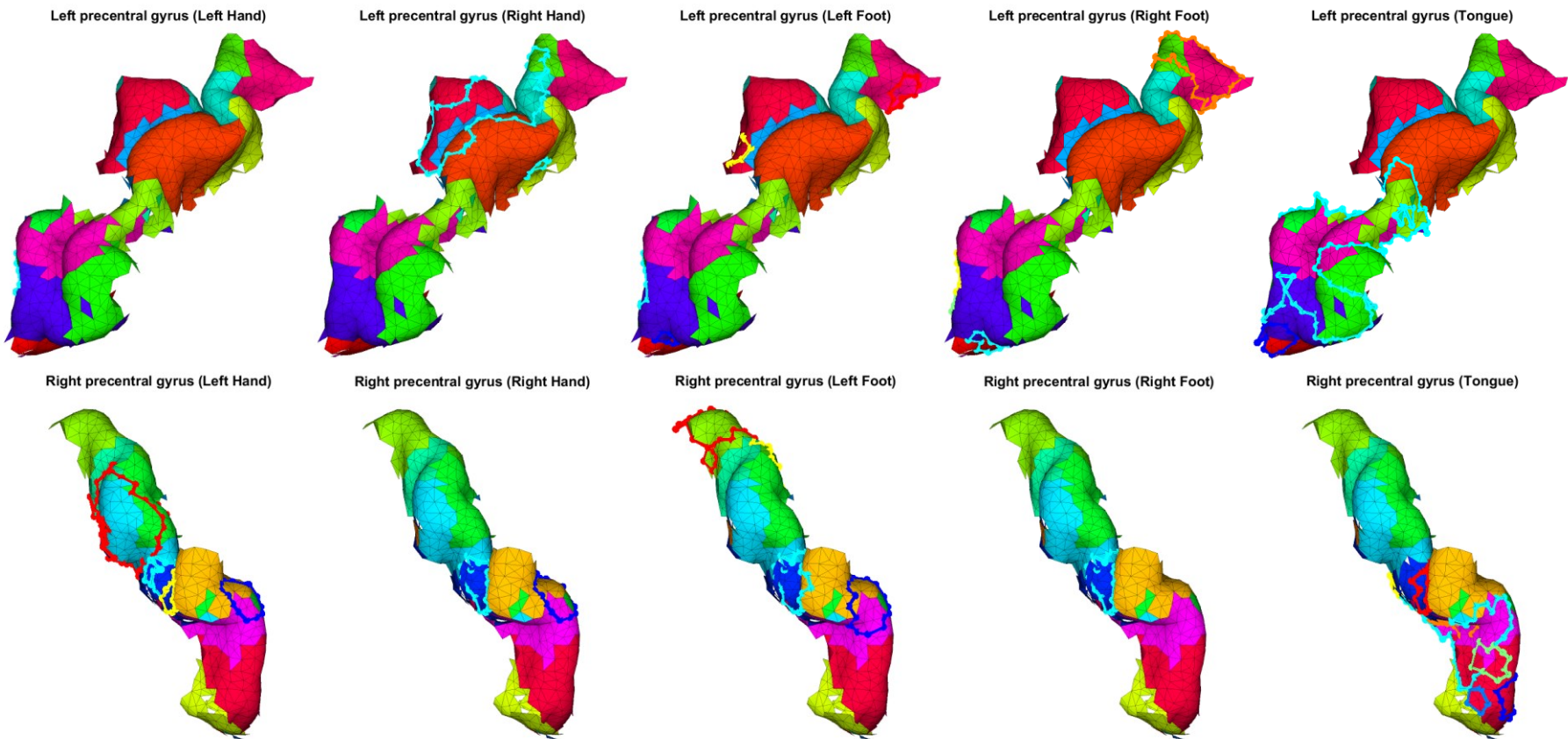
Right precentral gyrus (Tongue)



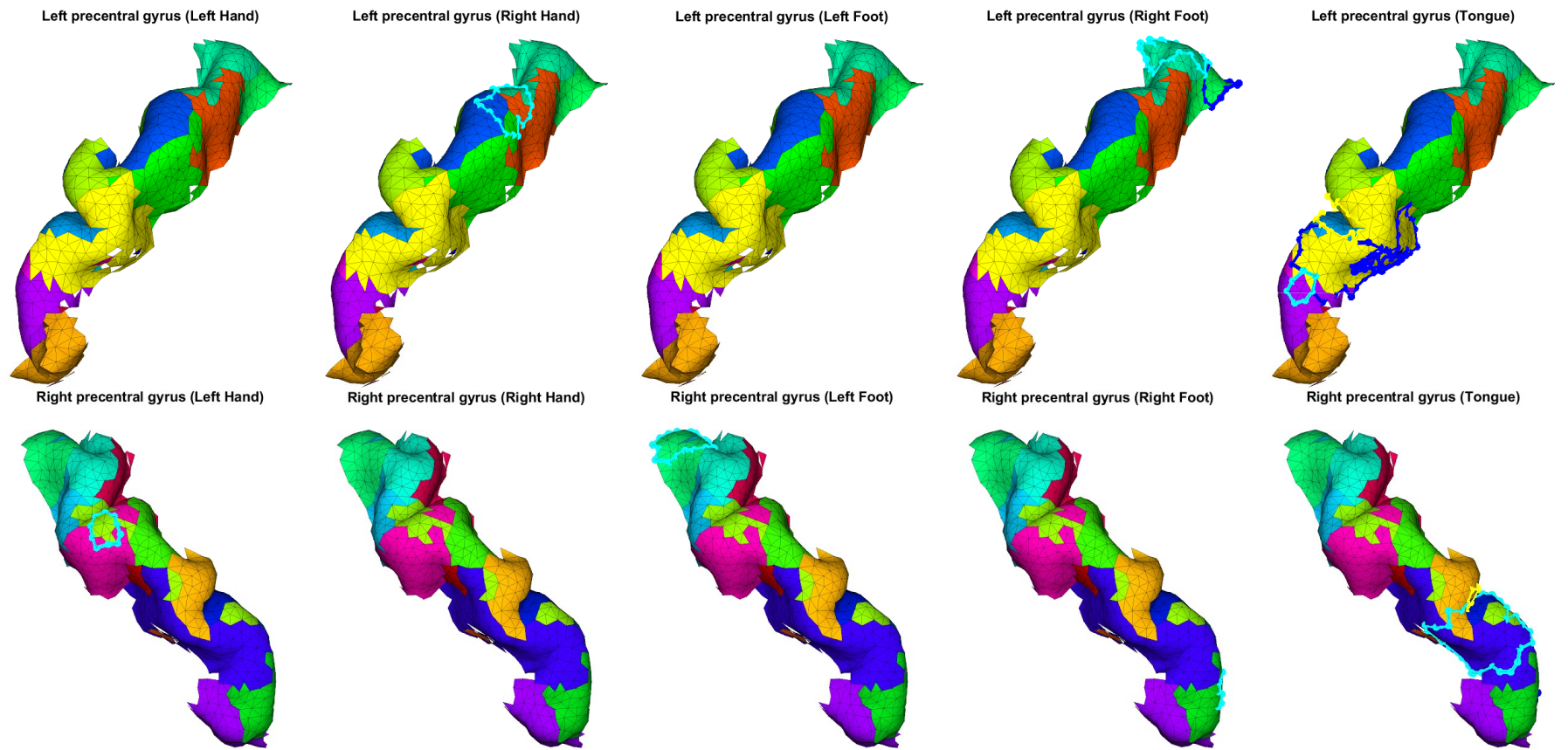
Participant: sub-07



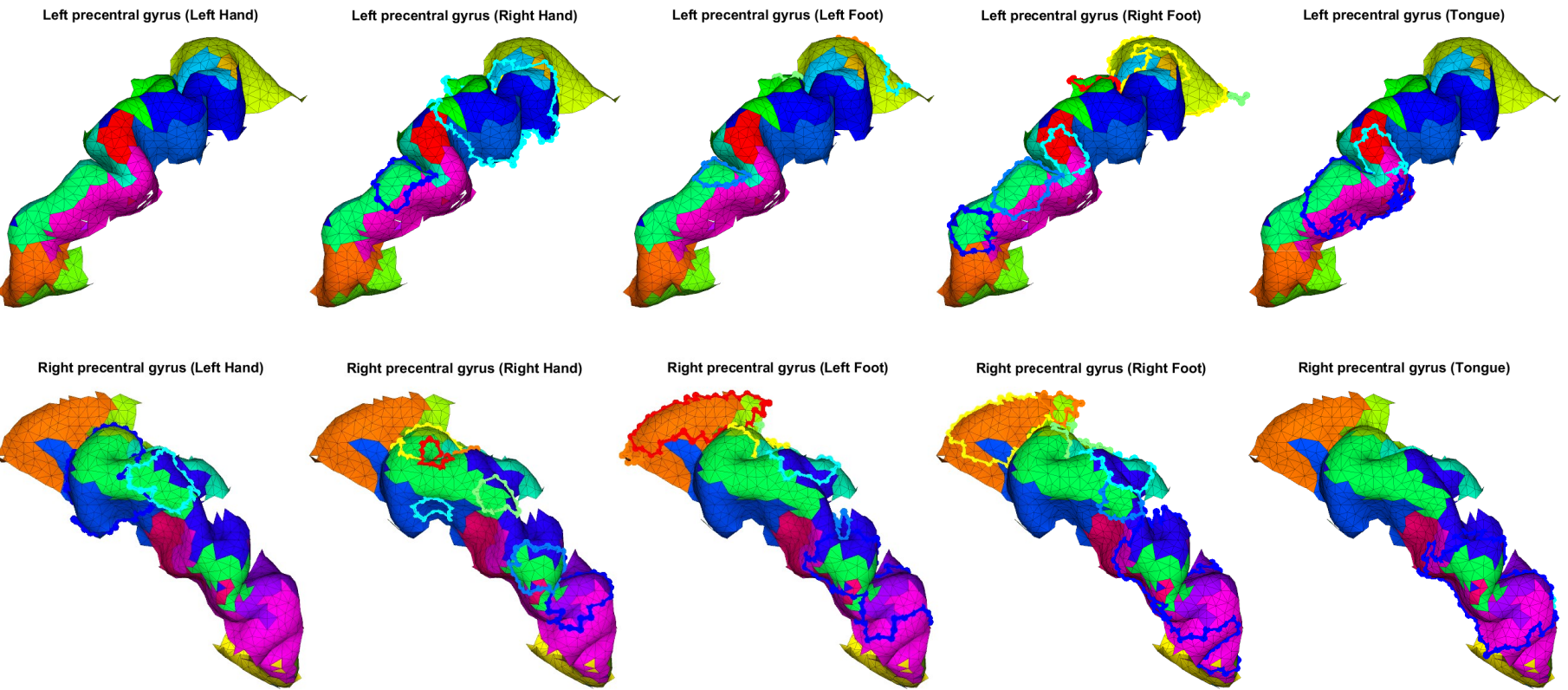
Participant: sub-08



Participant: sub-09

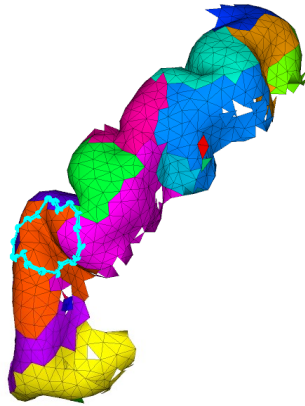


Participant: sub-11

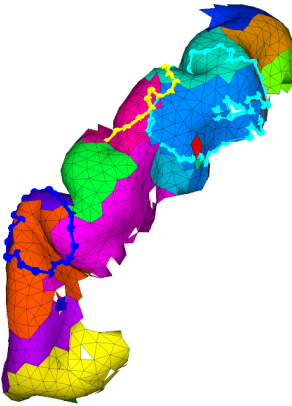


Participant: sub-12

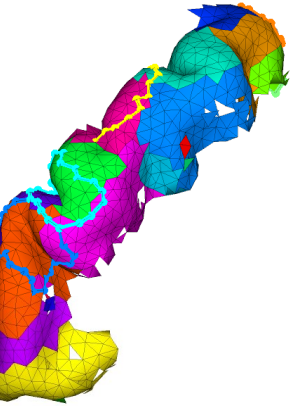
Left precentral gyrus (Left Hand)



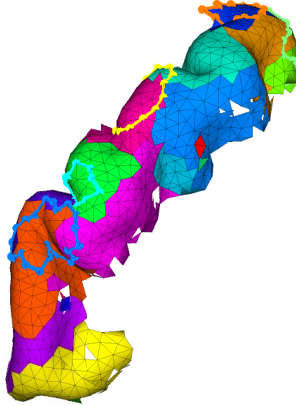
Left precentral gyrus (Right Hand)



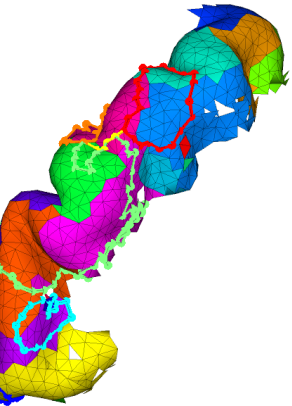
Left precentral gyrus (Left Foot)



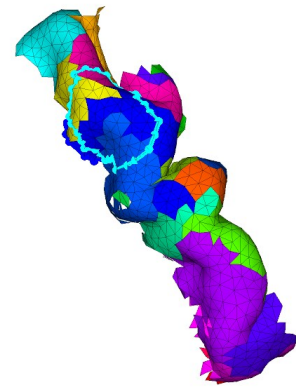
Left precentral gyrus (Right Foot)



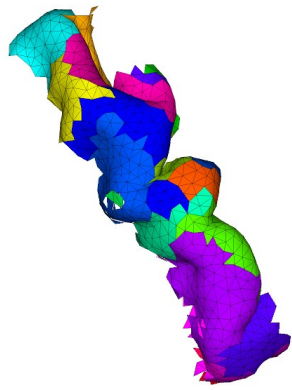
Left precentral gyrus (Tongue)



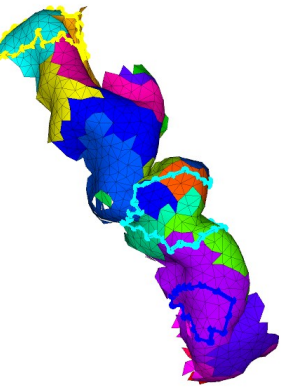
Right precentral gyrus (Left Hand)



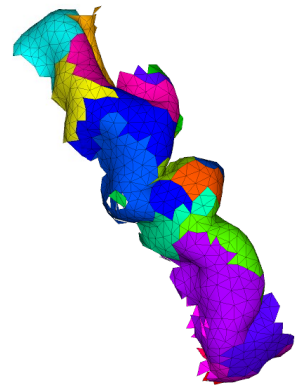
Right precentral gyrus (Right Hand)



Right precentral gyrus (Left Foot)



Right precentral gyrus (Right Foot)

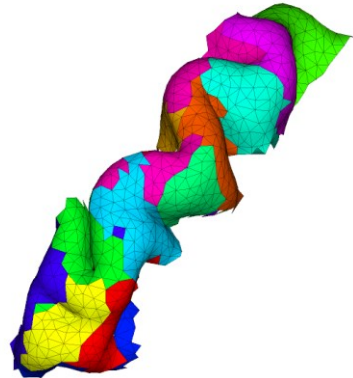


Right precentral gyrus (Tongue)

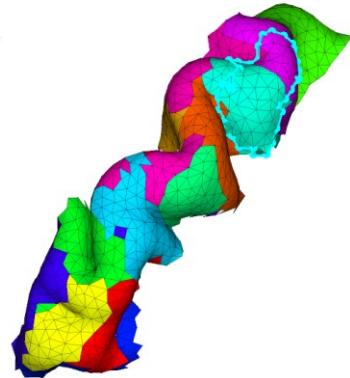


Participant: sub-13

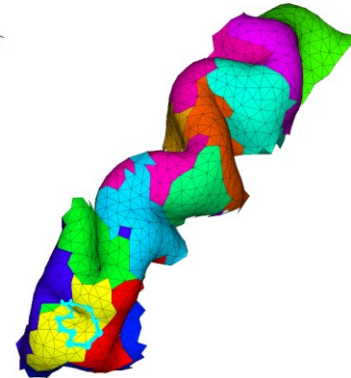
Left precentral gyrus (Left Hand)



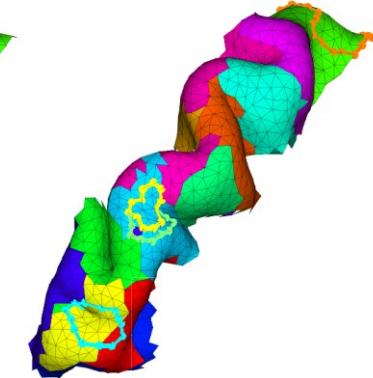
Left precentral gyrus (Right Hand)



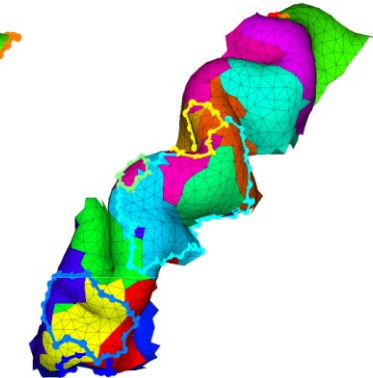
Left precentral gyrus (Left Foot)



Left precentral gyrus (Right Foot)



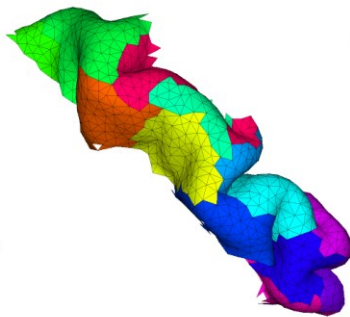
Left precentral gyrus (Tongue)



Right precentral gyrus (Left Hand)



Right precentral gyrus (Right Hand)



Right precentral gyrus (Left Foot)



Right precentral gyrus (Right Foot)

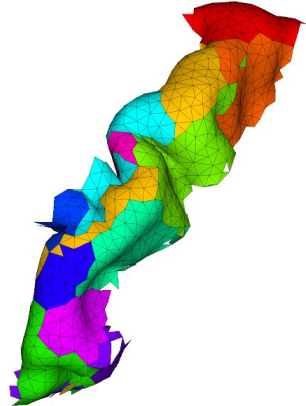


Right precentral gyrus (Tongue)

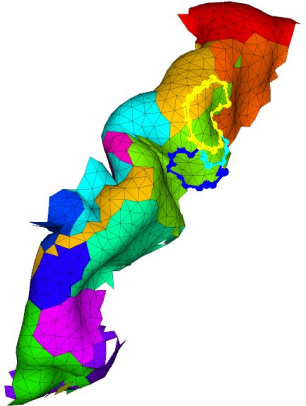


Participant: sub-14

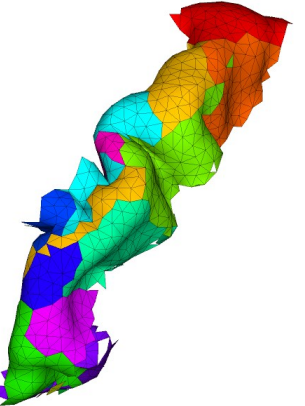
Left precentral gyrus (Left Hand)



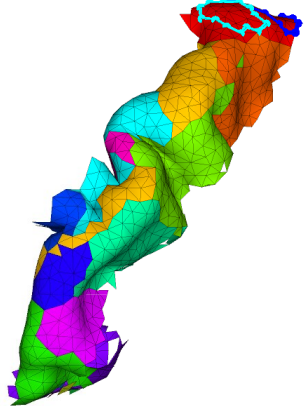
Left precentral gyrus (Right Hand)



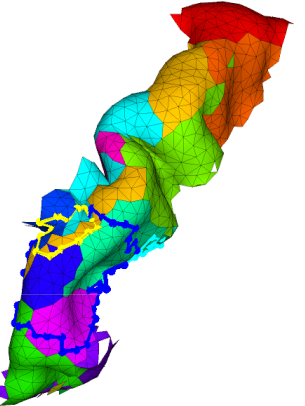
Left precentral gyrus (Left Foot)



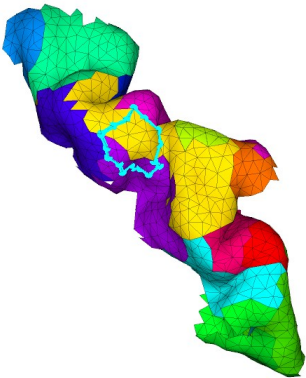
Left precentral gyrus (Right Foot)



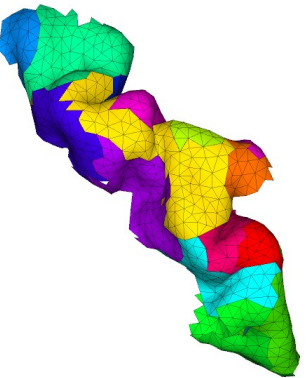
Left precentral gyrus (Tongue)



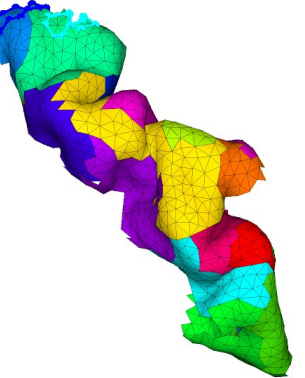
Right precentral gyrus (Left Hand)



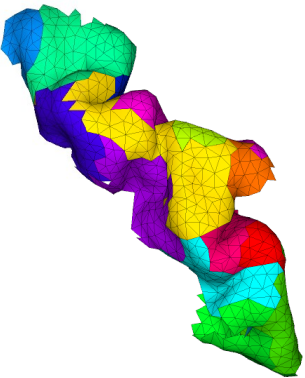
Right precentral gyrus (Right Hand)



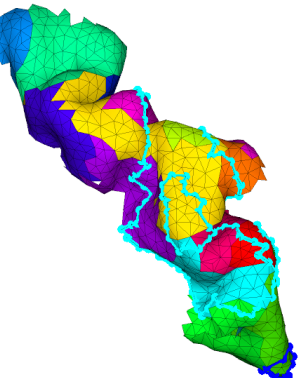
Right precentral gyrus (Left Foot)



Right precentral gyrus (Right Foot)



Right precentral gyrus (Tongue)



12 APPENDIX F

12.1 DISTRIBUTION OF QUANTITY OF ALL FUNCTIONAL AND STRUCTURAL MODULES

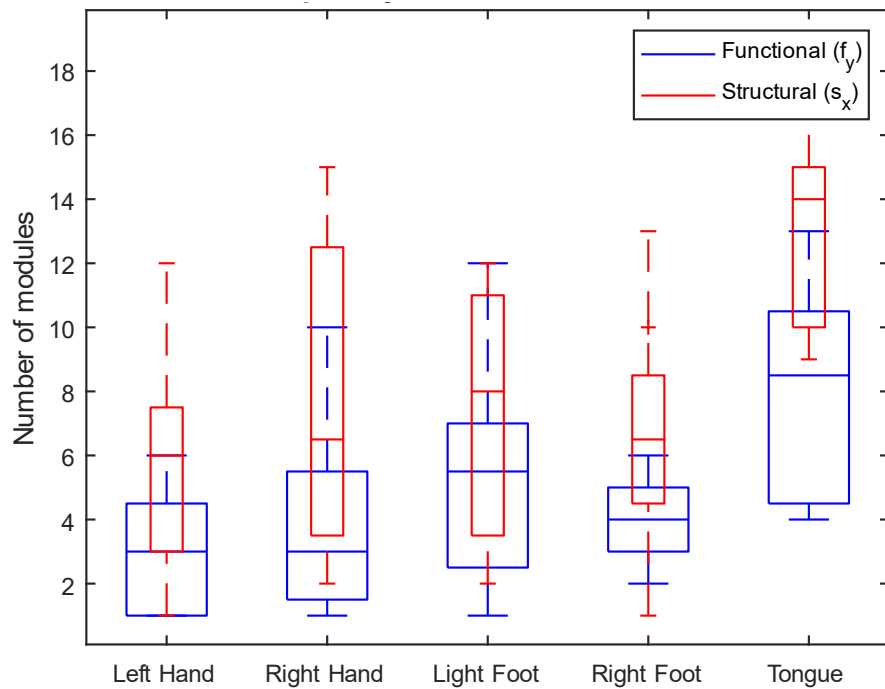


Figure 27: Boxplot showing the distribution in quantity of all (not limited to f_*) functional and structural modules that were elucidated during each task. Created by looping through results for each participant and counting the number of s_x and f_y per motor task.

12.2 NORMALISED COVERAGE OF f_y OVER s_x PER SUBJECT BY CONDITION

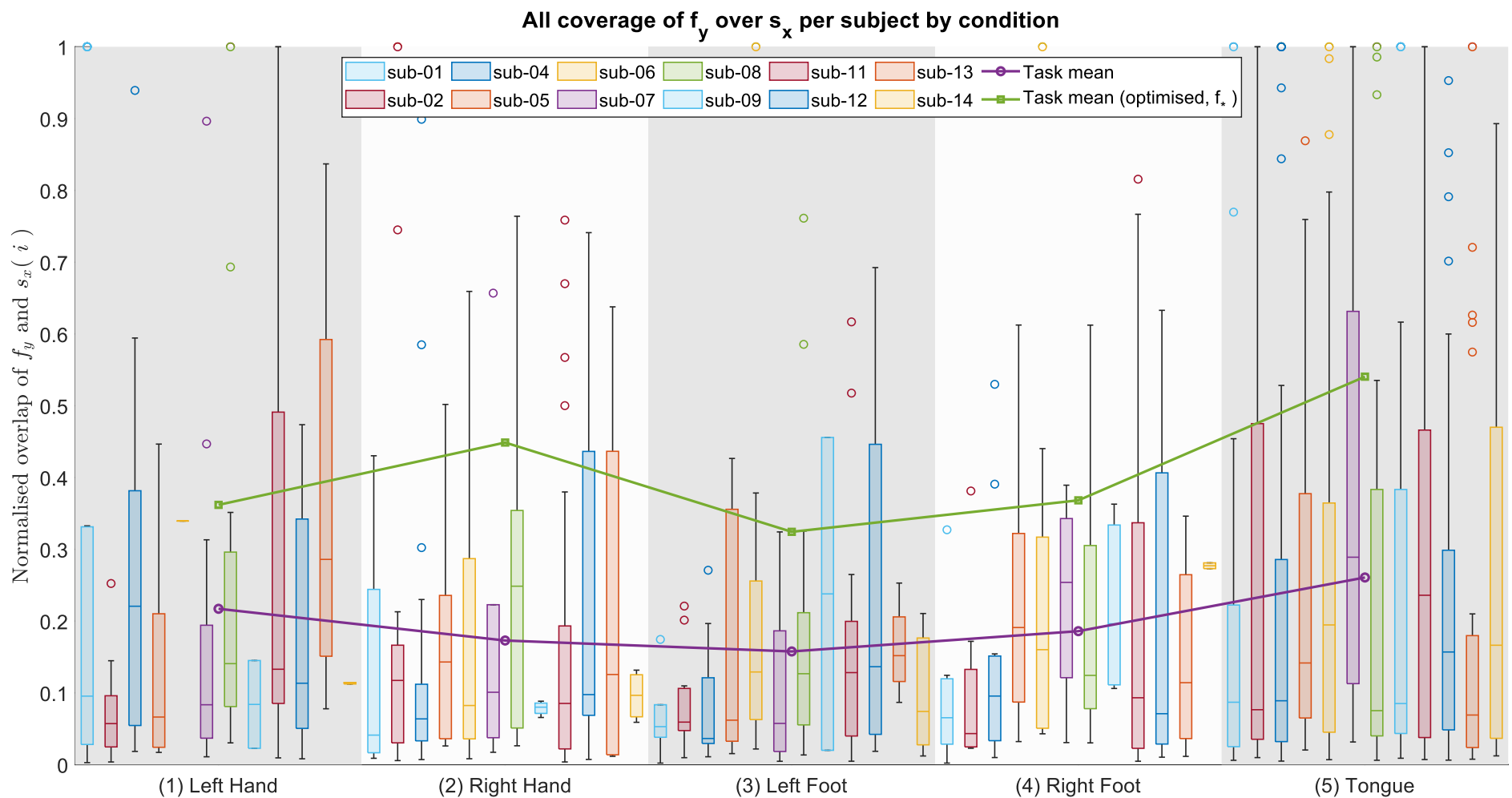


Figure 28: Boxplots for each motor task, showing the distribution of functional modules' (f_y) overlap with underlying structural modules (i), normalised by Equation: 6 and plotted per participant. Also plotted is a per-task mean of the structure-function overlap, both for f_y and f_* . Increases in i were found for all tasks, following our method of f^* selection.

13 ACKNOWLEDGEMENTS

First and foremost, I have to thank Professor Marcus Kaiser (University of Nottingham) for their supervision throughout this project. They offered support whenever it was needed, and responded very quickly to all emails. They have inspired me to consider continuing research in this field. Thank you!

I would also like to acknowledge the work of Peter Taylor, Yujiang Wang, and Marcus Kaiser. Without them, this work would have started without foundations.